

Modulating the Structural, Magnetic and Transport Properties of Mn_3Sn via Ni Substitution

A Dissertation Report for

PHGO-311 Dissertation

Credits: 8

Submitted in partial fulfilment of Master's Degree

M.Sc. in Physics

by

ELISHKA LISANNE VAZ

21P043047

Under the Supervision of

DR. ELAINE T. DIAS

School of Physical and Applied Sciences

Physics



GOA UNIVERSITY

Date: May 2023

Modulating the Structural, Magnetic and Transport Properties of Mn_3Sn via Ni Substitution

A Dissertation Report for

PHGO-311 Dissertation

Credits: 8

Submitted in partial fulfilment of Master's Degree

M.Sc. in Physics

by

ELISHKA LISANNE VAZ

21P043047

Under the Supervision of

DR. ELAINE T. DIAS

School of Physical and Applied Sciences

Physics



GOA UNIVERSITY

Date: May 2023

Examined by:

[Handwritten signatures of examiners]



Seal of the School

Declaration

I hereby declare that the data presented in this Dissertation report entitled, “Modulating the Structural, Magnetic and Transport Properties of Mn_3Sn via Ni Substitution”, is based on the results of investigations carried out by me in Physics at the School of Physical and Applied Sciences, Goa University under the Supervision of Dr. Elaine T. Dias and the same has not been submitted elsewhere for the award of a degree or diploma by me. Further, I understand that Goa University or its authorities will be not be responsible for the correctness of observations/experimental or other findings given the dissertation.

I hereby authorize the University authorities to upload this dissertation on the dissertation repository or anywhere else as the UGC regulations demand and make it available to any one as needed.



Elishka Lisanne Vaz

21P043047

Physics

School of Physical and Applied Sciences

Date: May 2023

Place: Goa University

Certificate

This is to certify that the Dissertation report entitled, “Modulating the Structural, Magnetic and Transport Properties of Mn_3Sn via Ni Substitution”, is a bonafide work carried out by Ms. Elishka Lisanne Vaz under my supervision in partial fulfillment of the requirements for the award of the degree of M.Sc. in the Discipline Physics at the School of Physical and Applied Sciences, Goa University.



Dr. Elaine T. Dias

Physics

Date: May 2023



Prof. Kaustubh R. S. Priolkar

Dean

School of Physical and Applied Sciences

Date: May 2023

Place: Goa University

Acknowledgment

It is said, that feeling gratitude and not expressing it is like wrapping a present and not giving it.

It gives me pleasure, at the end of the successful completion of my dissertation, to express my deepest and sincerest thanks to my guide, Dr. Elaine, for her invaluable guidance and constant support throughout the course of this work. She has mentored me patiently with her expertise, and her constant encouragement has been instrumental in shaping our research and helping me overcome difficulties along the way.

I would also like to extend my heartfelt thanks to the Dean of the School of Physical and Applied Science (SPAS), Goa University, Prof. Dr. Kaustubh R. S. Priolkar, and the Programme Director of Solid State Physics, Dr. Sudhir Cherukulappurath, for granting permission to use the necessary facilities and resources to carry out my work effectively.

I appreciate the assistance and help extended by the Ph.D. students, Nafi, Myren, Nandesh, Namita and Mahendra, and I also thank the non-teaching staff at SPAS for their technical assistance.

Lastly, but certainly not least, I would like to express my gratitude to my parents and sister. Their unwavering moral support during this demanding period has been invaluable.

Once again, I extend my sincere appreciation to all those who have contributed to the completion of this dissertation.

Contents

Declaration	i
Certificate	ii
Acknowledgement	iii
Contents	iv
List of Figures	vi
List of Tables	viii
1 Introduction	1
1.1 The Mn_3X Family of Compounds	2
1.2 Mn_3Sn	4
1.2.1 Crystal Structure	5
1.2.2 Magnetic Structure	6
1.3 Transition Metals Doped into the Mn_3Sn System	8
2 Experimental Methods	10
2.1 Sample Preparation	10
2.2 Characterization Techniques	16

<i>CONTENTS</i>	v
2.2.1 X-Ray Diffraction	16
2.2.2 Magnetization as a Function of Temperature	22
2.2.3 Resistivity	25
3 Results and Discussion	28
3.1 X-Ray Diffraction Analysis	28
3.2 Magnetization	32
3.3 Temperature Dependent Resistivity Measurements	36
References	38

List of Figures

1.1	Crystal and Magnetic Structure of Mn_3Sn	6
2.1	Binary Phase Diagram of $Mn-Sn$	11
2.2	Initial preparation of Manganese, Tin and Nickel.	13
2.3	Instruments used to prepare polycrystalline $Mn_{3-x}Ni_xSn_{0.96}$ alloys	14
2.4	Samples in Arc Furnace	15
2.5	Schematic of X-Ray Diffraction	17
2.6	Rigaku Smartlab X-Ray Machine	18
2.7	Schematic of a Josephson Junction in a DC SQUID	23
2.8	Superconducting pickup coil system in SQUID	24
2.9	Cryogenic Laboratory SQUID Magnetometer at MCL, Goa University	24
2.10	Sample inserted into the sample rod	25
2.11	Schematic of the Four Probe Arrangement	26
2.12	DC Resistivity Setup	27
2.13	Sample mounted for resistivity studies	27
3.1	Profile Fitting of Mn_3Sn using Le Bail Method	29
3.2	Rietveld Refinement of Mn_3Sn using FullProf Suite Software	30
3.3	Rietveld Refinement of $Mn_{3-x}Ni_xSn_{0.96}$ using FullProf Suite Software	31

3.4	Variation of lattice constants 'a' and 'c' with increasing Ni concentration	32
3.5	M v/s T for Mn_3Sn	33
3.6	M v/s T for $\text{Mn}_{3-x}\text{Ni}_x\text{Sn}_{0.96}$, $x = 0.1, 0.15, 0.2, 0.25$	35
3.7	Transition Temperatures	36
3.8	Resistivity data for $\text{Mn}_{3-x}\text{Ni}_x\text{Sn}$, $x = 0.1, 0.15, 0.2, 0.25$	37

List of Tables

2.1	Calculation of Molecular weights of each element	12
2.2	Weight Loss of the Samples Synthesized using Arc Melting	14
3.1	Rietveld parameters	31
3.2	Phase percentages	31

Chapter 1

Introduction

The existence of a variety of intriguing phenomena with potential applications in spintronic devices has led to a great deal of interest in magnetism in systems with noncollinear magnetic structures in recent years.^{1,2} As a result, antiferromagnetic spintronics is a rapidly growing field since it offers a number of benefits over the ferromagnets now in use.^{3,4} Insensitivity to external magnetic field perturbations, production of no stray fields, presence of rapid spin dynamics necessary for data preservation, and high-density memory integration are all characteristics of antiferromagnets.^{2,5-9}

Noncollinear chiral antiferromagnets have garnered the greatest attention among the numerous diverse antiferromagnetic^{10,11} or synthetic antiferromagnetic materials^{12,13}, thanks to their exceptional structural, magnetic, and electrotransport features. Some of these substances belong under the category of magnetic topological substances, which show how magnetic and electronic states of matter interact and serve as a crucial backdrop for revealing a variety of exotic phenomenon. The large anomalous Hall effect (AHE)^{14,15}, topological Hall effect (THE)¹⁶⁻¹⁹, spin Hall ef-

fect (SHE)²⁰, magneto-optical Kerr effect²¹, skyrmionic lattice²², thermoelectric effect^{23,24}, and so on are all produced by the kagome lattice, in which atoms are arranged in star-like formation, which causes geometrical frustration.

Due to their possible magnetic topological features, a number of kagome intermetallics have been extensively researched. For example, $Y\text{Mn}_6\text{Sn}_6$ is a rare-earth-based kagome system showing several competing magnetic orders and large THE²⁵, $\text{Co}_3\text{Sn}_2\text{S}_2$ is a magnetic Weyl semimetal showing giant anomalous Hall effect in addition to chiral anomaly²⁶, Mn_3Ge and Mn_3Sn are time-reversal symmetry-broken Weyl semimetals, and despite being antiferromagnets, show large anomalous Hall effect induced by the nonzero k-space Berry curvature^{27,28}, Fe_3Sn_2 which is a kagome ferromagnet generates skyrmionic bubbles in addition to the giant anomalous Hall effect^{29,30} and $\text{Gd}_3\text{Ru}_4\text{Al}_{12}$ possess a low-temperature skyrmion lattice induced by the magnetic frustration³¹.

1.1 The Mn_3X Family of Compounds

Noncollinear antiferromagnets (AFMs) based on Mn_3X ($X = \text{Sn}, \text{Ge}, \text{Ga}, \text{Rh}, \text{Ir}, \text{Pt}$) have attracted interest because, in contrast to the extensively studied collinear AFMs, these noncollinear AFMs exhibit significant anomalous Hall, anomalous Nernst, and magneto-optical Kerr effects at room temperature.

It has also been demonstrated that these noncollinear AFMs are home to a variety of exotic phenomena, including magnetic Weyl fermions, cluster octupole moment ordering, spin polarised current, and the magnetic spin Hall effect. These intriguing

ing results imply that the Berry curvature produced by the chiral spin structure has a significant impact on the charge and spin transport parameters. This makes the Mn_3X -based AFMs appealing for spintronics applications in addition to having potential for fundamental research.³²

$X = Ga, Ge, Sn$ are examples of Mn_3X compounds that crystallize with the hexagonal $D0_{19}$ structure. Theoretically, nonvanishing Berry curvature was predicted to cause Mn_3Sn and Mn_3Ge to exhibit large anomalous Hall effect, but band-structure computations show that these compounds exhibit a Weyl semimetal state with many Weyl points near the Fermi level. These theoretical calculations led to the discovery that Mn_3Sn and Mn_3Ge single crystals display substantial anomalous Nernst effect and large anomalous Hall effect, both of which are of the same order of magnitude as in ferromagnetic materials.⁹

It is not anticipated that antiferromagnets with no net magnetization will exhibit the anomalous Hall effect, which is widely known to scale with the magnetization of a ferromagnet. However, the non-vanishing Berry curvature of the chiral spin structure in the non-collinear triangular antiferromagnet hexagonal Mn_3Ge and Mn_3Sn results in a significant anomalous Hall effect. Theoretical models predict that the same spin structure also gives rise to a strong spin Hall effect. The chiral triangular antiferromagnet cubic Mn_3Ir , on the other hand, only exhibits a significant spin Hall effect and no signs of an anomalous Hall effect.³³

Tetragonally deformed cubic Mn_3Pt structures have been found to exhibit an in-

trinsically anomalous Hall effect. In epitaxially formed, face-centered cubic Mn_3Ir thin films, uncompensated Mn spins dominate the electrical transport behaviour, which results in a small anomalous Hall effect and negative magnetoresistance.³⁴ Epitaxial thin films of this material have been discovered to have a facet-dependent spin Hall effect (SHE), which results from a combination of spin-orbit coupling and symmetry breaking from the chiral antiferromagnetic structure. It has also been predicted to exhibit an intrinsic anomalous Hall effect. Large anomalous Hall effect have been experimentally seen in highly ordered bulk samples of Mn_3Sn and Mn_3Ge , both of which have demonstrated potential for anomalous Hall effect applications.³⁵

These compounds are interesting candidates for straintronic applications due to their strong piezomagnetism, large anomalous Hall effect, and metallic conductivity. In comparison to Mn_3Sn , Mn_3Ge may have even more significant piezomagnetic characteristics.³⁶ Large coercivity and abnormal Hall resistivity were observed in Mn_3Ga films, which were attributed to the frustrated spin structure of DO_{19} .³⁷

1.2 Mn_3Sn

A prime example of a material having a triangle spin structure is the antiferromagnetic semimetal Mn_3Sn , which is extensively discussed in the context of Weyl physics. The structure of the material's electronic bands, which strongly contribute to anomalous magneto-transport, is of special interest.³⁸⁻⁴³

Mn_3Sn offers a wide range of technological options for AFM spintronics at room temperature because of its exceptional magnetic, structural, and electrotransport ca-

pabilities.² Around room temperature, a sizable anomalous Hall effect with a triangular AFM spin arrangement is seen. A large anomalous Hall effect at room temperature²⁷, a large anomalous Nernst effect at room temperature³⁹, a large magneto-optical Kerr effect⁴⁴, magnetic and magnetic inverse spin Hall effects⁴⁵, and magnetic Weyl fermions⁴⁰ are examples of anomalous transport properties, while an angular-dependent Hall effect shows that the evolution of DWs with the magnetic field and magnetic anisotropy in Mn_3Sn also plays a significant role.^{46,47}

Since an antiferromagnet has no net magnetization, there should not be any anomalous Hall effect in a zero applied field. The antiferromagnet Mn_3Sn has been demonstrated to have a significant anomalous Hall conductivity²⁷ of the same order of magnitude as for ferromagnetic conductors. Before the discovery of Mn_3Sn , the anomalous Hall effect in antiferromagnets had not been observed.⁴⁷ Mn_3Sn 's complex physical properties may be inseparable from its unique structure. In the following subsections, we look at its crystal and magnetic structure and the properties that arise as a consequence.

1.2.1 Crystal Structure

Hexagonal $D0_{19}$ compounds belong to $P6_3/mmc$ (#194) space group.⁴⁸ In the case of the Mn_3X family, the six Mn atoms are located at the $6h$ Wyckoff positions $(x, 2x, 1/4)$. Stacked in an $ABAB$ sequence along the c-axis (at each $z = 1/4$ and $z = 3/4$ layers), the atoms form a kagome lattice, stabilized by the DM interaction, with triangles of Mn atoms along the edges of hexagons that host Sn atoms at their center, at $2c$ Wyckoff position $(1/3, 2/3, 1/4)$.^{27,47,49,50} Previous studies of Mn_3Sn

have found the lattice parameters to be $a = 5.67\text{\AA}$ and $c = 4.53\text{\AA}$.⁵¹ Each Mn atom has a spin magnetic moment of $\approx 3.0\mu_B$ per atom.⁵⁰

Geometric frustration of Mn atomic moments in this configuration results in a non-collinear AF structure with chiral 120° inverse triangular spin structure below ($T_N = 420K$).^{27,52-54} Weak ferromagnetism is also present as a result of small distortions in the lattice and the off-stoichiometry of the system.^{27,53} The low-temperature magnetic structure depends greatly on the elemental ratio of the Mn and Sn , annealing temperature and crystal growth techniques, with some studies reporting a helical spin structure and others a spin-glass state below $50K$.^{48,55-57}

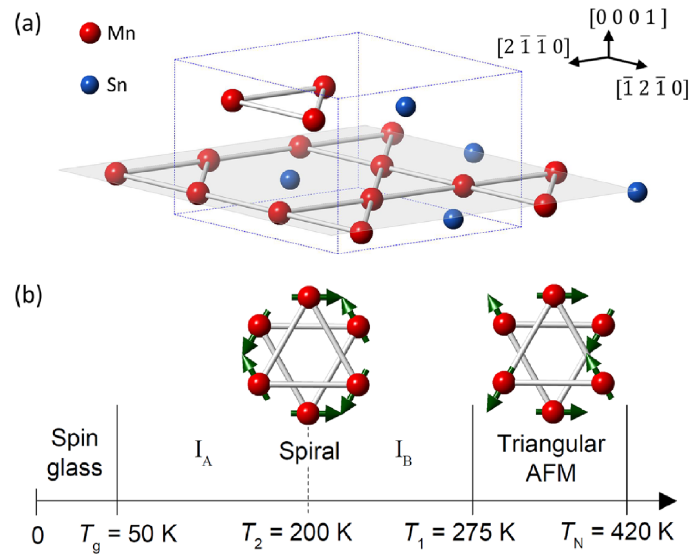


Figure 1.1: Crystal and Magnetic Structure of Mn_3Sn (taken from⁵⁸)

1.2.2 Magnetic Structure

Mn_3Sn is a non-collinear antiferromagnet (AFM) with a Néel temperature (T_N) of 420K, as shown by powder neutron diffraction.^{55,59} A geometrical frustration that results in an inverse triangular spin structure at 300K and a very small net ferromagnetic moment of $0.002 \mu_B/Mn$ atom is present in each of the structure's ab planes,

which are each made up of a slightly distorted kagome lattice of Mn moments each of $3\mu_B$. There is a minor deviation from the standard 120° structure, but all Mn moments lie on the ab plane and form a chiral spin texture with an opposing vector chirality. This roughly cancels the magnetic moment. Only one of the three moments in each Mn triangle in this inverse triangular configuration is parallel to the local easy-axis, thus this arrangement possesses orthorhombic symmetry.⁵⁵

As a result, it is believed that the weak ferromagnetic moment originated from the canting of the other two spins towards the local easy-axis. At $T_1 = 270\text{K}$, another magnetic transition takes place. Two models for the spin ordering have been put up: the spin configuration is spiral below T_1 and triangular above T_1 . The appearance of satellite reflections surrounding the fundamentals and the transfer of intensity from the fundamentals to the satellites serve as evidence that the interlayer ferromagnetic coupling is replaced by some sort of moment modulation along the c -axis direction below around 270 K .⁵³

The triangular structure has typically been described as undergoing a long-period helical modulation that is virtually independent of temperature down to 4.2K .⁵⁰ Composition and heat treatment have a significant impact on T_1 . The magnetic order of Mn_3Sn on a polycrystalline sample examined at low temperatures showed glassy ferromagnetism below $T_f = 31.8\text{K}$. Mn_3Sn single crystals subjected to a thorough neutron diffraction concludes that the compound is predominately AFM with weak ferromagnetism (WFM) between T_1 and T_N .^{51,53}

The Dzyaloshinskii-Moriya interaction results in the triangular antiferromagnetic configuration, and the WFM is the result of the distortion of the equilateral triangle and the non-stoichiometry of the compound in which a few Sn atoms have been substituted by Mn atoms.^{50,59,60} The inverse triangular spin state is reported to be maintained in as-grown crystals over a large temperature range (T) between T_N and 50K. Due to spin canting in the direction of the c axis, a cluster glass phase with a significant c -axis ferromagnetic component manifests at low temperatures.⁵⁸

1.3 Transition Metals Doped into the Mn_3Sn System

Recent research on Mn_3Sn has looked into how transition metals like Fe and Cr doping affect the material's characteristics. Studying the impact of Fe doping on Mn_3Sn led to the discovery of induced ferromagnetism and a shift in magnetic anisotropy below a specific temperature. At low temperatures, Fe doping also caused a metal-insulator transition and a rise in resistivity. Low-temperature topological Hall effect was caused by the magnetocrystalline anisotropy and competing magnetic interactions, which led to nontrivial spin texture. The topological characteristics of Mn_3Sn were significantly altered even at low concentrations of Fe doping.⁶¹

The study focusing on Cr doping showed that the antiferromagnetic structure of Mn_3Sn can be altered by tilting it out-of-plane, resulting in increased net moment, magnetocrystalline anisotropy energy, and Dzyaloshinskii-Moriya interaction perpendicular to the kagome plane. In AFM systems, this led to the coexistence of in-plane and out-of-plane exchange bias. The findings demonstrated that extra Cr doping increased the exchange bias field by more than ten times when compared to pure

Mn_3Sn , which produced perpendicular exchange bias. This finding of a significant exchange bias in an AFM system with a frustrated kagome structure opens up new avenues for research into how symmetry breaking and DMI are related.⁶²

The other study on Cr doping found that low-concentration Cr doping significantly increases the anomalous Hall conductivity, especially for modulation-doped samples at low temperature, which is attributed to the change in Fermi level caused by Cr doping, but does not significantly alter the structural or magnetic properties of Mn_3Sn .³²

In the present work, we have tried to investigate the effect of Ni substitution on the structural, magnetic and transport properties of Mn_3Sn . We report our investigations on the room temperature structure as well as the temperature dependent magnetic (5K to 390K) and transport properties (30K to 450K) of the $Mn_{3-x}Ni_xSn$ alloys.

Chapter 2

Experimental Methods

In this chapter, we first present detailed calculations of the stoichiometric weights of the constituent elements used to prepare the $Mn_{3-x}Ni_xSn$ alloys. The chapter then goes on to describe the two methods used to synthesize the alloys, i.e., the solid state reaction method and the arc melting method. Next, the working principles of the various characterization techniques, that is, x-ray diffraction, DC magnetization and four probe resistivity measurements are described.

2.1 Sample Preparation

Mn_3Sn contains Mn and Sn atoms in the ratio 3 : 1, or 75 : 25. According to literature⁵¹, Mn_3Sn hexagonal phase ($P6_3/mmc$) is only stable in the off-stoichiometric configuration of $Mn_{3+\delta}Sn$. Therefore to compensate for the mass loss and to take care of the high vapour pressure of manganese, an excess amount (0.65% by weight) of manganese over the stoichiometric amount was taken. Next, according to the $Mn-Sn$ binary phase diagram (fig. 2.1), a stable single phase Mn_3Sn alloy forms when the Sn concentration lies between 24 and 26. Thus to create a deficit of Sn , the ratio of

75 : 25 is modified to 75 : 24, or 3 : 0.96. Hence the stoichiometry of elements in a single formula unit chosen for this study has the general formula, $Mn_{(3-x)}Ni_xSn_{0.96}$, with $x = 0, 0.1, 0.15, 0.2, 0.25$.

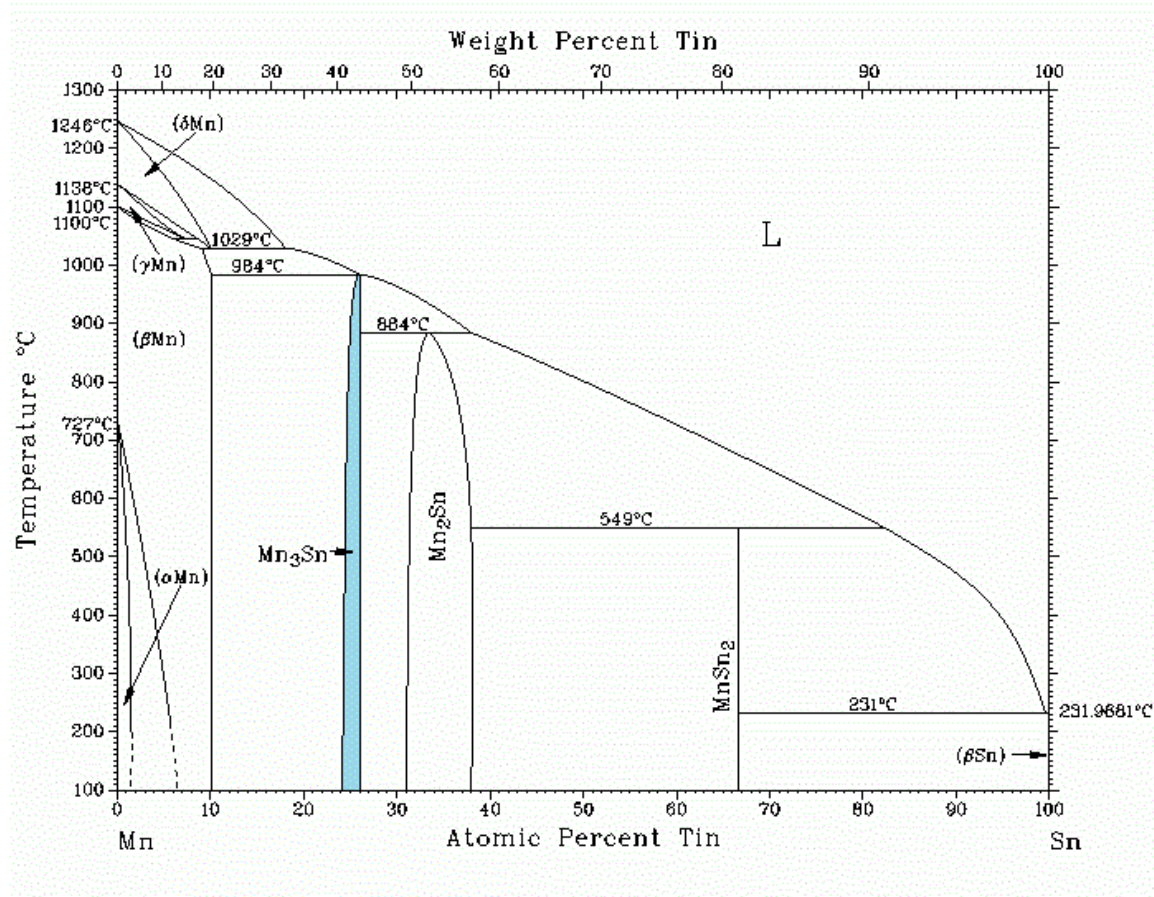


Figure 2.1: Binary Phase Diagram of $Mn-Sn$

Polycrystalline alloys of $Mn_{(3-x)}Ni_xSn_{0.96}$ were synthesized by arc melting the stoichiometric amounts of high purity constituent elements i.e. manganese (mol. wt. 54.938g/mol)(Alfa Aesar, manganese pieces, irregular, 99.9%), tin (mol. wt. 118.69g/mol) (Alfa Aesar, tin shot, 3mm, 99.99 +%) and nickel (mol. wt. 58.71g/mol) (Alfa Aesar). The weight of each element in a single chemical unit is calculated by multiplying the atomic weight by the stoichiometric number and then dividing it by the molecular weight of the compound.

For example, in $Mn_{2.9}Ni_{0.1}Sn_{0.96}$, the molecular weight of the compound is

$$Mol. wt. = 2.9 \times 54.938 + 0.96 \times 118.69 + 0.1 \times 58.71 = 283.8812 g$$

The weights of Mn , Sn , and Ni in this compound are therefore,

$$Amt\ of\ Mn = \frac{2.9 \times 54.938}{283.8812} = 0.6735 g$$

$$Amt\ of\ Sn = \frac{0.96 \times 118.69}{283.8812} = 0.4816 g$$

$$Amt\ of\ Ni = \frac{0.1 \times 58.71}{283.8812} = 0.0248 g$$

Stoichiometric weights of the constituent elements taken to prepare $\sim 1.2 g$ of $Mn_{3-x}Ni_xSn$ alloys are presented in table. 2.1.

Table 2.1: Calculation of Molecular weights of each element

Formula Unit	Molecular Weight (g)	Amt. of Mn (g)	Amt. of Sn (g)	Amt. of Ni (g)
$Mn_3Sn_{0.96}$	283.504	0.6976	0.4823	0
$Mn_{2.9}Ni_{0.1}Sn_{0.96}$	283.8812	0.6735	0.4816	0.0248
$Mn_{2.85}Ni_{0.15}Sn_{0.96}$	284.0698	0.6614	0.4813	0.0372
$Mn_{2.8}Ni_{0.2}Sn_{0.96}$	284.2584	0.6494	0.4810	0.0496
$Mn_{2.75}Ni_{0.25}Sn_{0.96}$	284.447	0.6374	0.4807	0.0619

For this, nickel pieces were cut from the block, and the weights of Mn and Sn were back calculated to maintain stoichiometry. The required amount of manganese was taken and put in metal cleaner and placed in an ultrasonicator (fig. 2.3a) for 15 minute intervals, 3-4 times, and cleaned intermittently with isopropyl alcohol. At the end, it was again cleaned in acetone in the ultrasonicator for another 10-15 minutes. Tin beads was flattened for holding the Mn and Ni pieces (see fig 2.2).

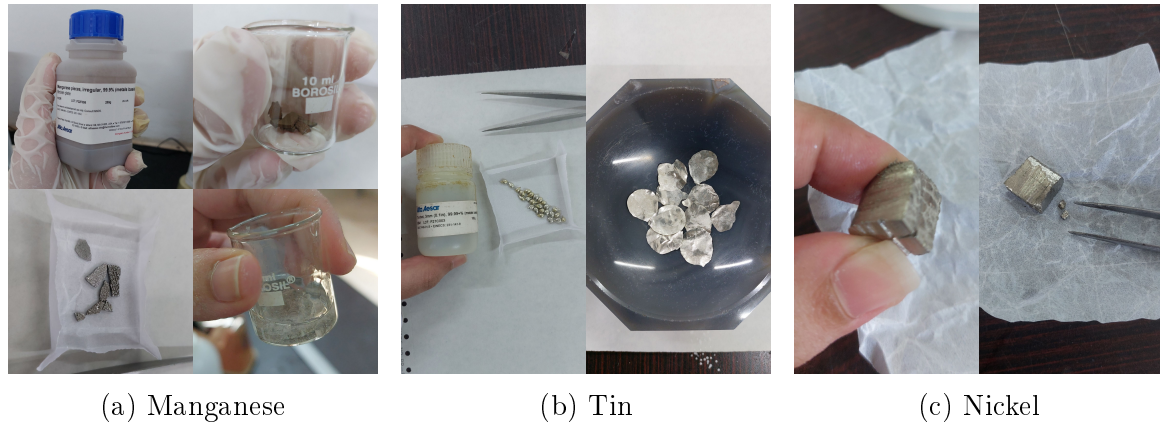


Figure 2.2: Initial preparation of Manganese, Tin and Nickel.

The samples were synthesized using the arc melting process, in argon atmosphere using a Centorr arc furnace. For this, the constituent elements were placed in the copper hearth, depending on the vapour pressure of the individual elements and the chamber was evacuated to a pressure of 10^{-3} torr for about 5 minutes followed by filling the chamber with argon gas to a pressure slightly above atmospheric pressure for about 3 minutes followed by flushing. This process is repeated three times and finally the alloy constituents are melted by generating an arc by striking the electrode on the copper hearth. To ensure a better homogeneity, the samples were melted multiple times by flipping the sample bead. The arc current was kept at 60A for the first melt, and 70-80A for subsequent melts (see fig. 2.3c and fig. 2.4).

The sample beads obtained from arc melting were first weighed to calculate weight loss (see table 2.2), then cut into halves using a low speed diamond cutter (fig. 2.3b) and sealed in separate quartz tubes under vacuum (10^{-5} bar) for annealing. The tubes were placed in a Carbolite furnace (fig. 2.3d) and heated from room temperature to 800°C for three days, before quenching in ice cold water.

Table 2.2: Weight Loss of the Samples Synthesized using Arc Melting

Sample	Weight Before (<i>g</i>)	Weight After (<i>g</i>)	Weight Loss %
$Mn_3Sn_{0.96}$	1.1923	1.1653	2.3
$Mn_{2.9}Ni_{0.1}Sn_{0.96}$	1.1835	1.1530	2.6
$Mn_{2.85}Ni_{0.15}Sn_{0.96}$	1.4484	1.4258	1.6
$Mn_{2.8}Ni_{0.2}Sn_{0.96}$	1.3211	1.2851	2.8
$Mn_{2.75}Ni_{0.25}Sn_{0.96}$	1.4113	1.3944	1.2



(a) Ultrasonicator



(b) Low Speed Diamond Cutter



(c) Arc Furnace



(d) Carbolite Furnace

Figure 2.3: Instruments used to prepare polycrystalline $Mn_{3-x}Ni_xSn_{0.96}$ alloys



Figure 2.4: Samples in Arc Furnace

For x-ray diffraction and magnetization studies, one of the annealed halves of each sample was ground in an agate mortar and pestle to a fine powder. For resistivity studies, a thin slice of the other half was cut to obtain a thin, almost rectangular bar.

Further, in order to obtain single crystals from the polycrystalline alloys, smaller pieces from Mn_3Sn and $Mn_{2.75}Ni_{0.25}Sn_{0.96}$ were sealed in smaller quartz tubes under vacuum (10^{-5} bar) for a second annealing. The tubes were placed in a Carbolite furnace and followed an annealing process as follows: heat from room temperature $1000^{\circ}C$ at a rate of $100^{\circ}C$ per hour and hold for 6 hours. Then the temperature was lowered to $600^{\circ}C$ at a rate of $2^{\circ}C$ per hour, followed by air quenching to room temperature.

Prior to this synthesis method, an attempt was made to prepare single crystals using the self-flux method, with chemical formula $Mn_{(7-x)}Ni_xSn_3$, with $x = 0, 0.1, 0.15, 0.2, 0.25, 0.3$. The constituent elements were the same as used in the polycrystalline samples above, except that nickel powder was used instead of pieces. The tin was flattened and cut into small pieces and then the elements were ground together

in an agate mortar and pestle and then sealed in quartz tubes (10^{-5}) bar. The tubes were placed in a Carbolite furnace and were heated from room temperature to 1000°C at a rate of 100°C per hour and held there for 6 hours. The temperature was then brought down to 900°C at the rate of 1.2°C per hour and then air quenched to room temperature.

2.2 Characterization Techniques

2.2.1 X-Ray Diffraction

X-rays are electromagnetic waves whose wavelengths range from 0.1\AA to 100\AA , which is of the same order of magnitude as the lattice constants of crystals, and it is this attribute which makes x-rays useful in the analysis of crystal structures. The method of determining a crystal's atomic and/or molecular structure using x-rays is called x-ray crystallography.^{63,64}

The internal structure of the crystal causes the incident X-ray beam to diffract. Parallel atomic planes in the crystal specularly reflect the incident waves, with each plane reflecting only a tiny fraction of the radiation. When there is constructive interference from the reflections from parallel planes, a diffraction pattern is produced that depends on the crystal structure and wavelength.

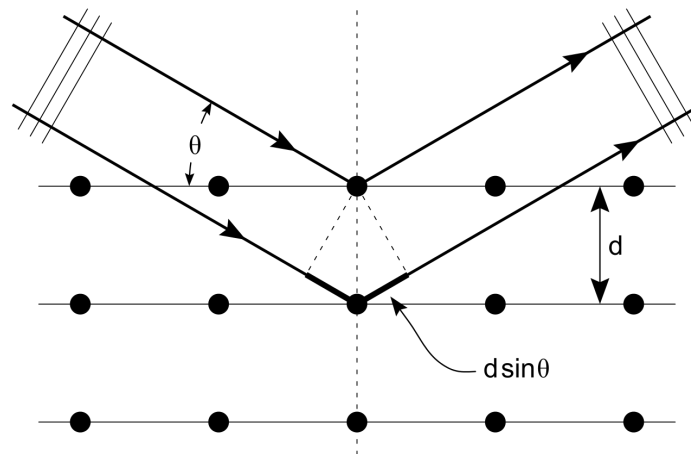


Figure 2.5: Schematic of X-Ray Diffraction (By Hydrargyrum - Own work, CC BY-SA 3.0, https://commons.wikimedia.org/w/index.php?title=File:Bragg_diffraction_2.svg&oldid=484440777)

Consider parallel lattice planes spaced d apart, as in figure 2.5. The radiation is incident in the plane of the paper. The path difference for rays reflected from adjacent planes is $2d \sin \theta$ where θ is measured from the plane. Constructive interference of the radiation from successive planes occurs when the path difference is an integral number n of wavelengths λ , leading to the Bragg condition, $2d \sin \theta = n\lambda$. This is the Bragg law, which can be satisfied only for wavelength $\lambda \leq 2d$. Although the reflection from each plane is specular, for only certain values of θ will the reflections from all periodic parallel planes add up in phase to give a strong reflected beam. The beams show a sharp peak in the intensity of the scattered x-rays. The density of electrons within the crystal can be visualized in three dimensions by measuring the angles and intensities of the diffracted beams. The mean positions of the atoms in the crystal, their chemical bonds, their crystallographic disorder, and other details can all be inferred from this electron density.

Experimental Details

The sample beads that were air quenched were cooled to room temperature before being ground to a fine powder for x-ray diffraction studies. The powder of each sample was placed on a glass slide that is used as a sample holder and spread out in a circular motion to avoid any preferred orientations. X-ray diffraction patterns were recorded using $\text{Cu K}\alpha$ radiation ($\lambda = 1.5418 \text{ \AA}$) on a Rigaku SmartLab diffractometer (see fig.2.6).



Figure 2.6: Rigaku Smartlab X-Ray Machine at MCL, Goa University

During a typical measurement, monochromatic x-rays generated from a rotating anode x-ray generator are collimated to concentrate before being directed towards the sample. When the x-ray beam hits an atom of the crystalline substance the

electrons in the atom begin to oscillate with the same frequency as the incoming beam and some of the incident photons are deflected away. When the scattering of x-ray photons occurs only due to transfer of momentum, that is there is no loss of energy (elastic scattering) the x-rays carrying information about the electron distribution in materials are used for diffraction experiments. Constructive interference patterns of diffracted waves from different atoms thus consists of sharp peaks (maxima) with the same symmetry as in the distribution of atoms. A scan through the range of $20^\circ \leq 2\theta \leq 80^\circ$ in steps of 0.02° allows to obtain all possible diffraction directions of the lattice that are required to examine the phase formation and purity of the compounds formed.

Refinement of Data

X-ray diffraction patterns recorded for all $Mn_{3-x}Ni_xSn$ alloys were first refined using the Le Bail method was refined using the Le Bail Method and qualitatively analyzed using Rietveld Refinement technique, both in the FULLPROF Suite software. A few details on both the methods is given below.

Le Bail Method Le Bail analysis is a powder diffraction profile fitting technique used for crystallographic structural determination. The method is used to extract intensities from powder diffraction data and is particularly useful for determining atomic structure and refining the unit cell. The algorithm involves refining the unit cell, the profile parameters, and the peak intensities to match the measured powder diffraction pattern. The Le Bail method is based on least squares analysis and involves fitting parameters such as the unit-cell parameters, peak width parameters, peak shape parameters, and instrumental zero error. It is not necessary to know the

structural factor and associated structural parameters, since they are not considered in this type of analysis. Le Bail analysis is easily integrated into Rietveld analysis software and is a part of a number of programs. It is a powerful tool for crystallographic structural determination, allowing for the identification of phase transitions in high pressure and temperature experiments, and provides a quick method for refining the unit cell, which allows better experimental planning.

Rietveld Refinement Today's most used powder X-ray diffraction (XRD) refining approach is based on a method Hugo Rietveld proposed in the 1960s.⁶⁵ The Rietveld approach uses experimental data to fit a computed profile (with all structural and instrumental characteristics). It makes use of the non-linear least squares method and necessitates the accurate initial approximation of a large number of free parameters, such as peak form, unit cell dimensions, and coordinates of every atom in the crystal structure. Some parameters can still be reasonably refined while being conjectured. By using powder x-ray diffraction patterns (PXRD), one can further refine the crystal structure of a powder material. The quality of the data, the model's quality (including initial approximations), and the user's experience strongly influence the refinement's performance.

Rietveld refinement requires a crystal structure model and does not provide a means of generating one on its own. However, it can be used to find structural details missing from a partial or complete ab initio structure solution, such as unit cell dimensions, phase quantities, crystallite sizes/shapes, atomic coordinates/bond lengths, micro strain in crystal lattice, texture, and vacancies.

In order to calculate intensities of the peaks in the diffraction patterns recorded for the samples, a hypothetical structural model adopting constraints imposed by the crystallographic space group $P6_3/mmc$, corresponding fractional coordinates, atomic site occupancies and roughly accurate lattice constants was generated. Parameters of the model generated were iteratively refined using the Least-Square method based on the minimization of the residual S between experimental and calculated patterns.

$$S = \sum_i w_i |y_{io} - y_{ic}|^2 \quad (2.1)$$

where w_i is a suitable weight given by

$$(w_i)^{-1} = \sigma_i^2 = \sigma_{ip}^2 + \sigma_{ib}^2 \quad (2.2)$$

σ_{ip}^2 and σ_{ib}^2 represent the standard deviation associated with a peak and background intensity (y_{ib}) respectively. (y_{io}) represents the intensity observed in the i^{th} step and (y_{ic}) gives the sum of contributions from neighbouring Bragg reflections. (y_{ic}) can be calculated as

$$y_{ic} = s \sum_k m_k L_k |F_k|^2 G(\Delta\theta_{ik}) + y_{ib} \quad (2.3)$$

where the terms s , m_k , L_k , F_k and G represent the scale factor, multiplicity factor, Lorentz polarization coefficient for the reflection k , structure factor and reflection profile function. $\Delta\theta_{ik} = 2\theta_i - 2\theta_k$, $2\theta_k$ and y_{ib} represent the position of the calculated Bragg peak and background intensity. $|F_K|$ depends upon position of each atom j

within each Miller plane,

$$F_{hkl} = \sum_j N_j f_j e^{2\pi i(hx_j + ky_j + lz_j)} e^{-B \frac{\sin^2 \theta}{\lambda^2}} \quad (2.4)$$

where N_j represents the site occupancy, B the temperature factor, f_j the structural factor and x_j, y_j, z_j the coordinates of the j^{th} atom. A good fit is characterized by reliability factors,

$$R_p = \frac{\sum |y_{io} - y_{ic}|}{\sum y_{io}} \quad (2.5)$$

$$R_{wp} = \left[\frac{\sum w_i |y_{io} - y_{ic}|^2}{\sum w_i y_{io}^2} \right]^{1/2} \quad (2.6)$$

$$R_{Bragg} = \frac{\sum ||I_{ko} - I_{kc}|}{\sum I_{ko}} \quad (2.7)$$

$$R_{exp} = \left[\frac{(N - P)}{\sum w_i y_{io}^2} \right] \quad (2.8)$$

$$\chi^2 = \frac{\sum w_i |y_{io} - y_{ic}|^2}{(N - P)} \quad (2.9)$$

R_p of the diffraction pattern (minimized during fitting procedures), R_{wp} (weighted to emphasize intense peaks over background), R_{Bragg} (tries to modify the R for a specific phase), R_{exp} (estimates the best value R for a data set) and reduced χ^2 (Goodness of fit).

2.2.2 Magnetization as a Function of Temperature

The magnetization as a function of temperature for all the samples was recorded using a ‘Superconducting Quantum Interference Device’ or SQUID magnetometer. SQUID magnetometer is a highly sensitive device widely used in materials science to study the magnetic properties of materials. The fundamental phenomenon behind the device is

the Josephson effect, wherein a supercurrent can penetrate through a thin insulating barrier between two superconductors, called a Josephson Junction, shown in fig. 2.7. It is a quantum tunnelling effect involving the coherent tunnelling of Cooper pairs through the barrier.

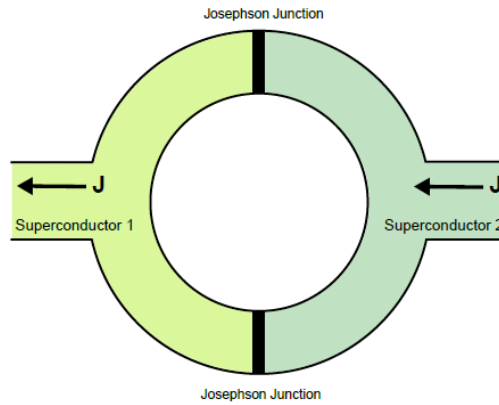


Figure 2.7: Schematic of a Josephson Junction in a DC SQUID

The device consists of a superconducting loop containing one or more Josephson junctions, which are made of two superconducting electrodes separated by a thin insulating barrier. When a magnetic field is applied to the loop, the phase difference between the two superconducting electrodes changes, resulting in a change in the current flowing through the junction.

A DC SQUID is built with two Josephson junctions and a DC current is applied to this device. The supercurrent through each Josephson junction depends on the phase difference between the complex order parameters of the superconductors that form the two halves of the ring. The flux through the ring leads to asymmetric phase differences across the two junctions which causes an interference pattern in the current across the device. A bias current is applied that is greater than the critical current of the junctions (the maximum current that can flow without dissipation, i.e., volt-

age) so that a voltage appears across the device which depends on the flux in the ring.

The SQUID does not see flux directly from the sample. A superconducting pickup coil system is used to couple the flux from the sample to the SQUID. Figure 2.8 shows a superconducting pickup coil with inductance L_P and an input coil (also superconducting) with inductance L_i that couples to the SQUID.

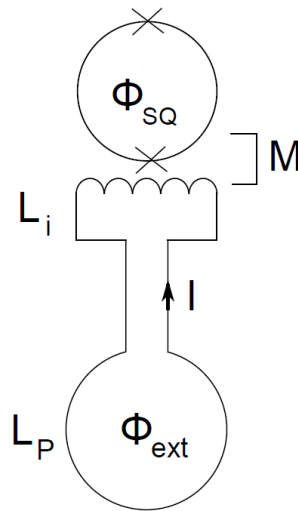


Figure 2.8: Superconducting pickup coil system in SQUID



Figure 2.9: Cryogenic Laboratory SQUID Magnetometer at MCL, Goa University



Figure 2.10: Sample inserted into the sample rod

2.2.3 Resistivity

A material's electronic structure determines its electrical resistivity, which is independent of its geometry. It is determined through a measurement of resistance, which depends on sample geometry and size. Further, to investigate the transport properties of the prepared alloys, a standard D.C. four probe setup in an Advanced Research Systems Inc, Closed Cycle Refrigerator (CCR) was used. The electrical resistivity was measured in zero applied magnetic field, in the temperature range between 30 K and 450 K.

The resistivity apparatus consists of a sample holder with four equidistant copper contacts. In the four probe arrangement, four collinear probes (probe size \ll sample dimensions) make an electrical contact with the sample. The inner two probes measure potential difference $+V$ and $-V$, whereas the outer probes conduct current $+I$ and $-I$.

See figure 2.11 for reference. From the measured potential difference and the known source current, the resistivity of the sample can be determined.⁶⁶ Rectangular bars with dimensions in the millimetre range were cut from the sample and used for the measurements.

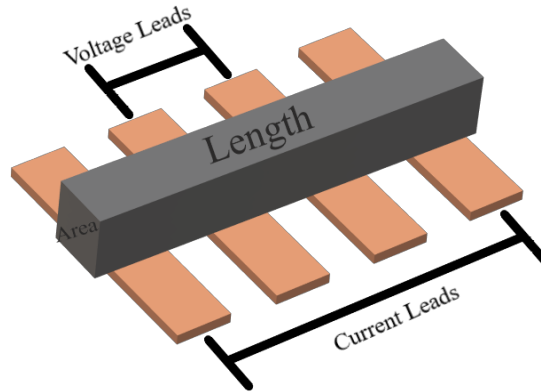


Figure 2.11: Schematic of the Four Probe Arrangement

Using G-varnish as an adhesive the sample is mounted onto this holder which is placed directly on the cold head of a He closed loop cycle refrigerator. G-varnish provides a good thermal contact while electrically isolating the sample from the rest of the sample holder. A colloidal solution of silver paint is used to make electrical contact between the probes and the sample.

The entire system is first evacuated and cooled to low temperatures. 100mA current is then passed using a Keithley 6221 DC and AC current source and the voltage developed is measured using a Keithley 2182A nanovoltmeter, as a function of temperature. The temperature of the sample was controlled using a Lakeshore 325 temperature controller. The data acquisition was carried in the cooling and warming cycles in the temperature range of 30K to 450K. Figure 2.12 shows the DC resistivity setup and figure 2.13 shows the manner in which the sample is fixed to the four probes.



Figure 2.12: DC Resistivity Setup, SPAS Lab, Goa University



Figure 2.13: Sample mounted for resistivity studies

The resistance of the sample is calculated using Ohm's law, $V = IR$, and the resistivity ρ of the samples is calculated from the dimensions of the rectangular bar cut, according to the relation $\rho = RA/l$, A being the area of cross section and l being its length.

Chapter 3

Results and Discussion

Polycrystalline samples of $Mn_{3-x}Ni_xSn$ prepared using the arc melting techniques were analyzed for the present study. First, the phase formation and purity of the samples was analyzed using an X-ray diffractometer. The temperature dependent magnetic behavior of all prepared alloys was then characterized using a SQUID magnetometer. Finally, temperature dependent electrical resistivity behavior of all samples was obtained using the four probe resistivity method. The obtained data is presented in this section.

3.1 X-Ray Diffraction Analysis

In order to check for phase formation and purity of the prepared $Mn_{3-x}Ni_xSn$ ($x = 0, 0.1, 0.15, 0.2, 0.25$) alloys, room temperature x-ray diffraction patterns were recorded using Cu K_α ($\lambda = 1.5418 \text{ \AA}$) radiation on a Rigaku SmartLab X-ray diffractometer. A scan through the range of $20^\circ \leq 2\theta \leq 80^\circ$ in steps of 0.02° allows to obtain all possible diffraction directions of the lattice that are required to examine the phase formation and purity of the compounds formed.

All patterns were first fitted using the Le Bail method. Figure 3.1 illustrates the Le Bail fitted pattern recorded for the Mn_3Sn alloy.

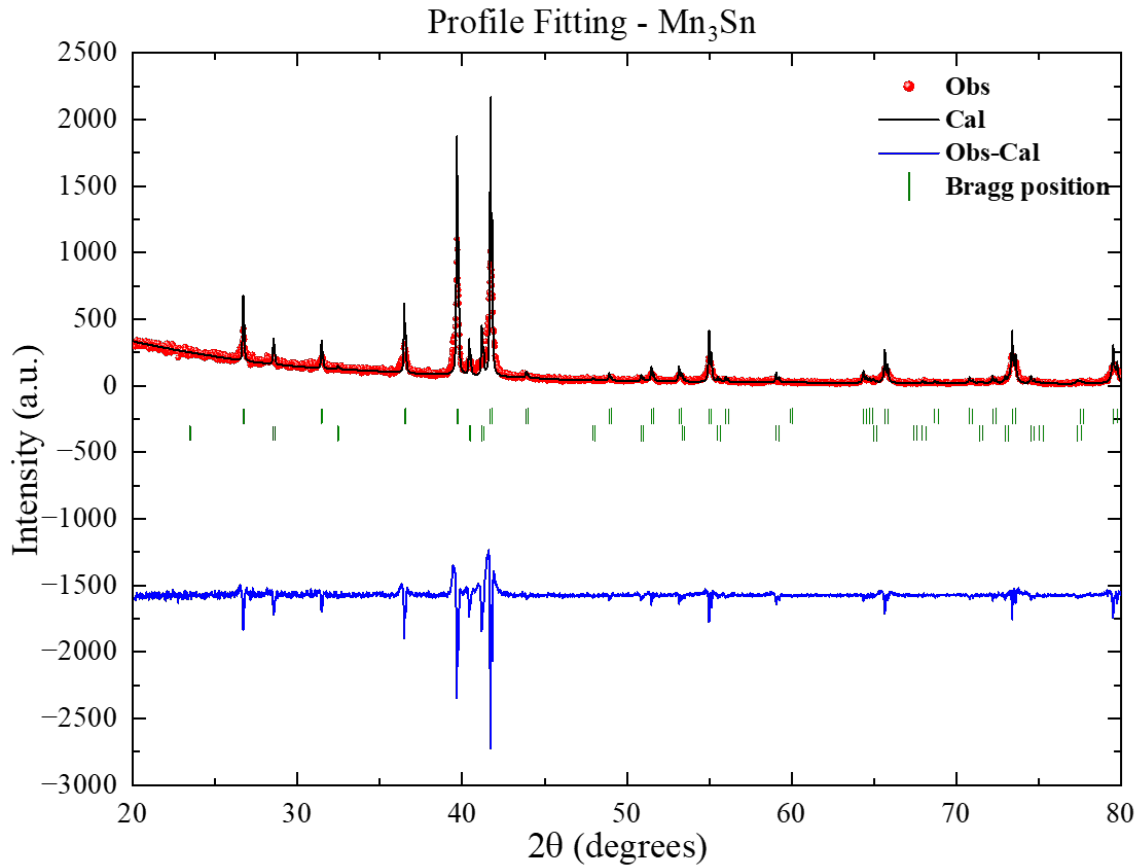


Figure 3.1: Profile Fitting of Mn_3Sn using Le Bail Method

Further, a qualitative analysis of all XRD patterns was carried out using Rietveld refinement technique in the FullProf Suite software. As seen in figure 3.2, the prepared Mn_3Sn alloy consists of a Mn_3Sn phase (97%) and a minor Mn_2Sn phase (3%). The crystallographic structure of the two phases were identified as hexagonal with the space group $P6_3/mmc$. The refined lattice parameters indicated in the figure (see fig. 3.4) show a fair agreement with those reported in literature.⁶¹ Theoretically, the highest intensity peak should be (201) but in this case we observed the (002)

peak to be the most intense one which could be only fitted by assigning the preferred orientation factor. The Rietveld analysis also yields an off-stoichiometric composition of $Mn_{3.026}Sn_{0.96}$ for the prepared polycrystalline sample.

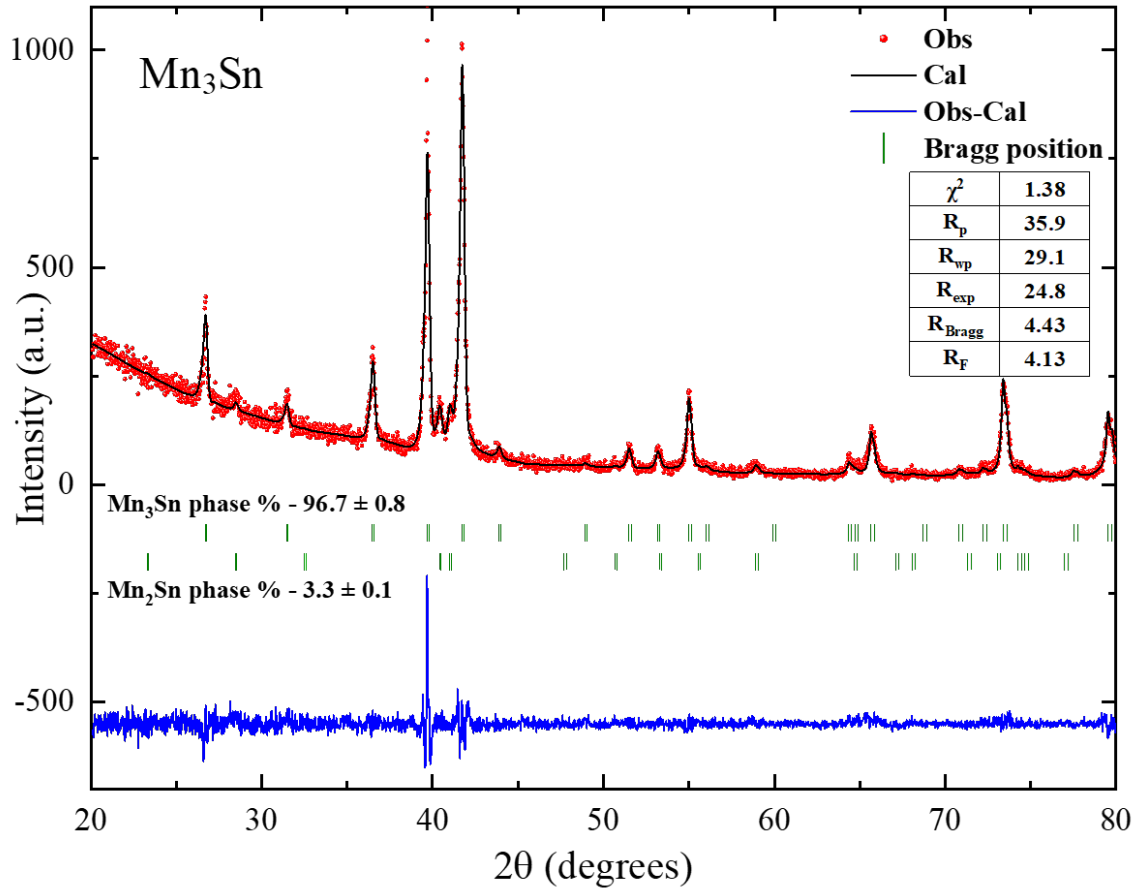


Figure 3.2: Rietveld Refinement of Mn_3Sn using FullProf Suite Software

Results from a similar analysis carried out on the *Ni* doped samples highlighted in fig. 3.3 suggest that all prepared alloys contain a minor $P6_3/mmc$ Mn_2Sn phase along with the desired hexagonal $P6_3/mmc$ Mn_3Sn phase. The Rietveld refined parameters and phase fractions obtained from this analysis are summarized in tables 3.1 and 3.2.

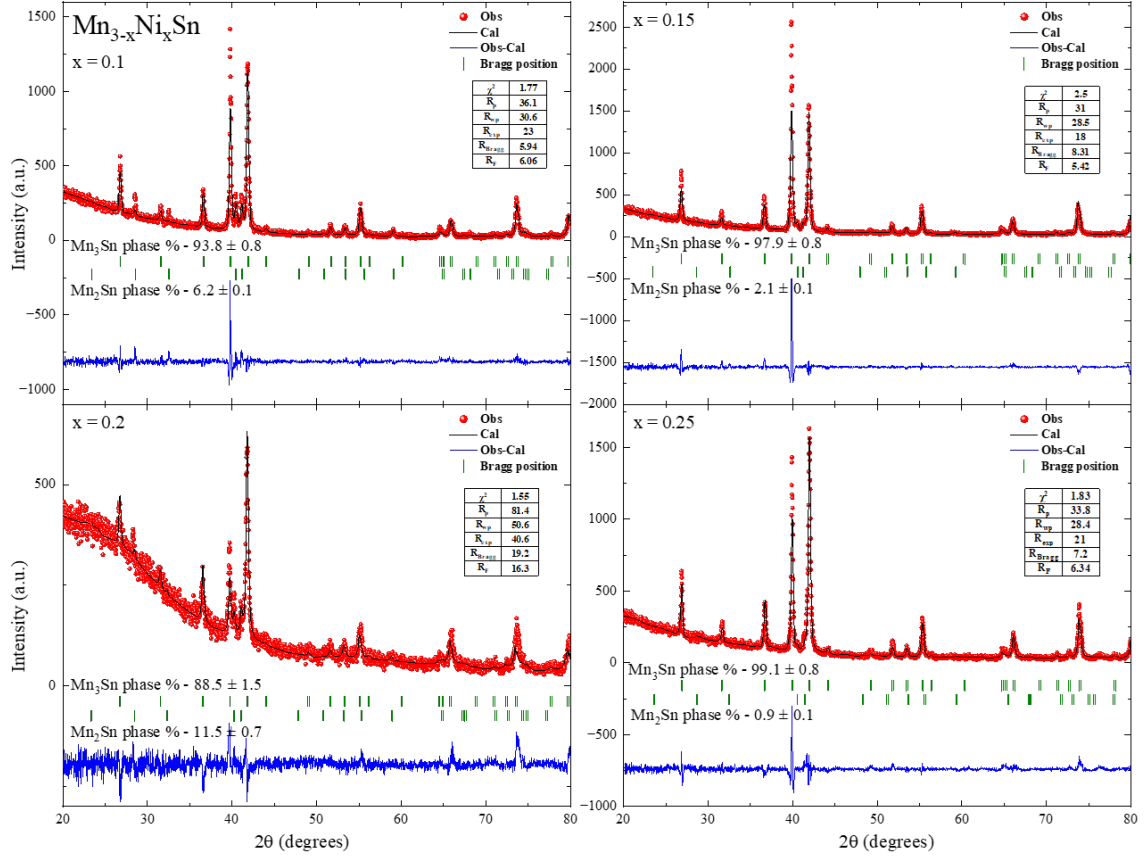


Figure 3.3: Rietveld Refinement of $Mn_{3-x}Ni_xSn_{0.96}$ using FullProf Suite Software, for $x = 0.1, 0.15, 0.2, 0.25$

Table 3.1: Rietveld parameters

Parameter	$Mn_3Sn_{0.96}$	$Mn_{2.9}Ni_{0.1}Sn_{0.96}$	$Mn_{2.85}Ni_{0.15}Sn_{0.96}$	$Mn_{2.8}Ni_{0.2}Sn_{0.96}$	$Mn_{2.75}Ni_{0.25}Sn_{0.96}$
χ^2	1.38	1.77	2.50	1.55	1.83
R_p	35.9	36.1	31.0	81.4	33.8
R_{wp}	29.1	30.6	28.5	50.6	28.4
R_{exp}	24.8	23.0	18.0	40.6	21.0
R_{Bragg}	4.43	5.94	8.31	19.20	7.20
$RF - factor$	4.13	6.06	5.42	16.30	6.34

Table 3.2: Phase percentages

Phase	$Mn_3Sn_{0.96}$	$Mn_{2.9}Ni_{0.1}Sn_{0.96}$	$Mn_{2.85}Ni_{0.15}Sn_{0.96}$	$Mn_{2.8}Ni_{0.2}Sn_{0.96}$	$Mn_{2.75}Ni_{0.25}Sn_{0.96}$
Mn_3Sn	96.72 ± 0.80	93.80 ± 0.84	97.93 ± 0.78	88.47 ± 1.46	99.13 ± 0.78
Mn_2Sn	3.28 ± 0.11	6.20 ± 0.14	2.07 ± 0.09	11.53 ± 0.66	0.87 ± 0.09

The graphical representation of lattice parameter variation as a function of the nickel concentration in fig. 3.4 highlights a systematic decrease as the concentration of Ni increases from $x = 0$ to $x = 0.25$. This decrease in lattice parameters with

nickel substitution at the *Mn* site can be attributed to the larger atomic radius of manganese atoms (140 pm empirical) as compared to that of nickel atoms (135 pm empirical). The discontinuity observed for the $x = 0.2$ alloy is most likely due to the presence of a larger Mn_2Sn impurity phase.

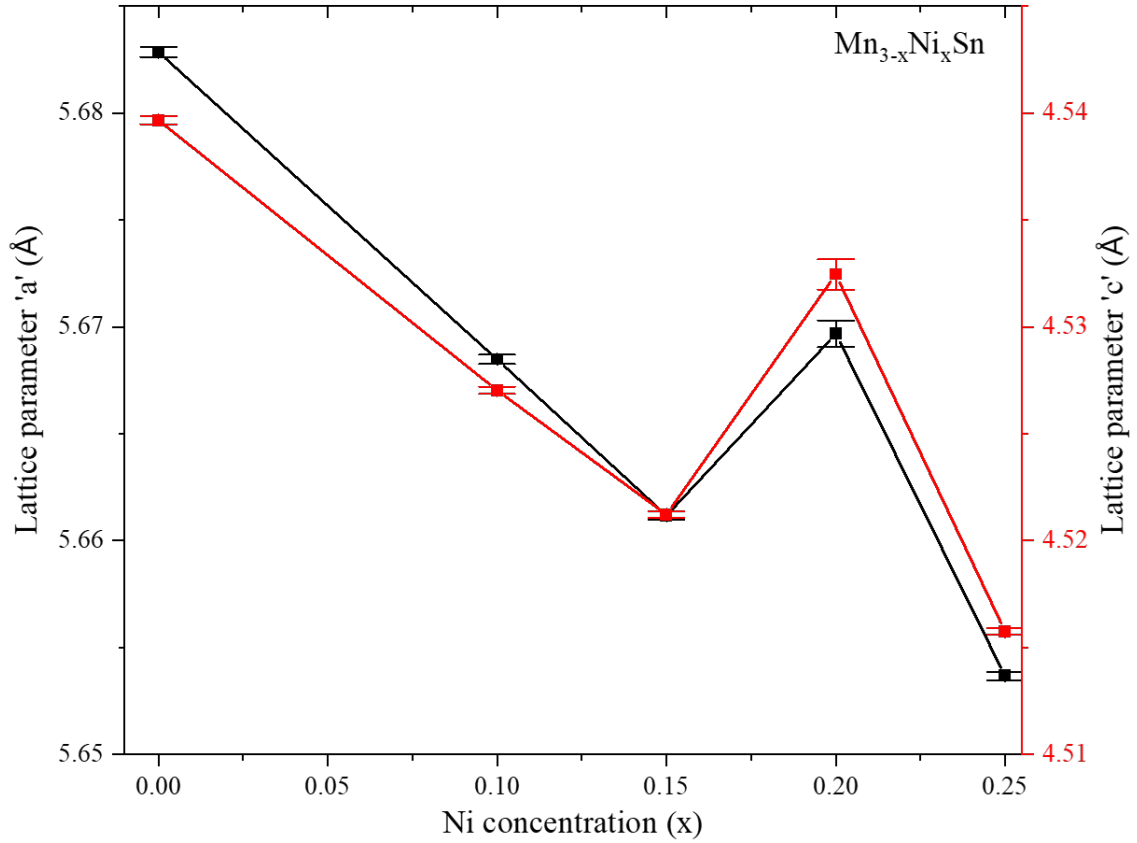


Figure 3.4: Variation of lattice constants 'a' and 'c' with increasing Ni concentration

3.2 Magnetization

The magnetization as a function of temperature of all the samples were recorded using a Cryogenic Laboratory SQUID magnetometer in the temperature range 5K to 390K, in an applied magnetic field of 0.01T. For this, about 15mg of fine powder of each of the samples was packed in a capsule, which was then inserted into a straw attached to the sample rod, was used for the measurements.

In order to carry out these measurements, the sample is first cooled from room temperature in zero applied magnetic field down to the lowest temperature (5K). Then a magnetic field of 0.01T was applied and data was recorded while warming to 390K. The data recorded during this cycle is referred to as the Zero Field Cooled (ZFC) data. The sample is then cooled back to 5K in the same applied magnetic field and no data was recorded. On reaching 5K, with the field of 0.01T still on, data was recorded while warming the sample upto 390K. This is the field cooled warming or FCW data.

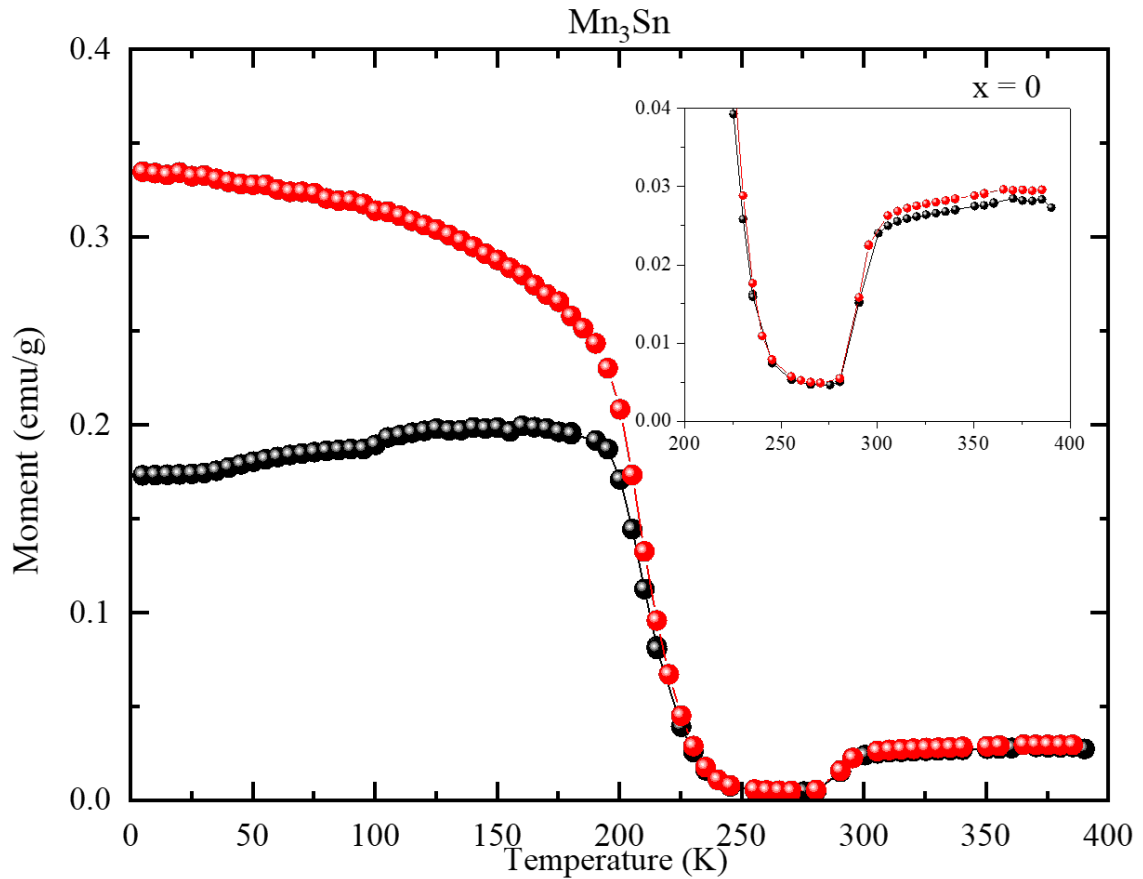


Figure 3.5: M v/s T for Mn_3Sn

The magnetization v/s temperature data recorded for the Mn_3Sn alloy in figure 3.5 is consistent with earlier magnetic and neutron diffraction studies. Mn_3Sn is an

antiferromagnet (AFM) with a Néel temperature T_N above 400K. As the sample is cooled, the compound undergoes a magnetic transition at $T_1 = 290\text{K}$. This transition corresponds to the magnetostructural phase transition from the triangular antiferromagnetic structure to the modulated phases.

After this change there is initially no difference between ZFC and FCW curves, implying that the structure below T_1 is still antiferromagnetic. As the temperature decreases below $T_2 = 215\text{K}$, the magnetization again increases. This transition can be to the anisotropy change of double helix magnetic structures. With further decrease in temperature, a slight drop in magnetization observed around 40K in the ZFC curve is indicative of the glassy ferromagnetic-like state reported for the alloy. The discrepancy between ZFC and FCW data curves also confirms the same. An analysis of the low temperature glassy state would require further frequency dependent a.c. susceptibility measurements.

A similar analysis of the temperature dependent magnetic properties measured for the *Ni* doped samples is given in figure 3.6.

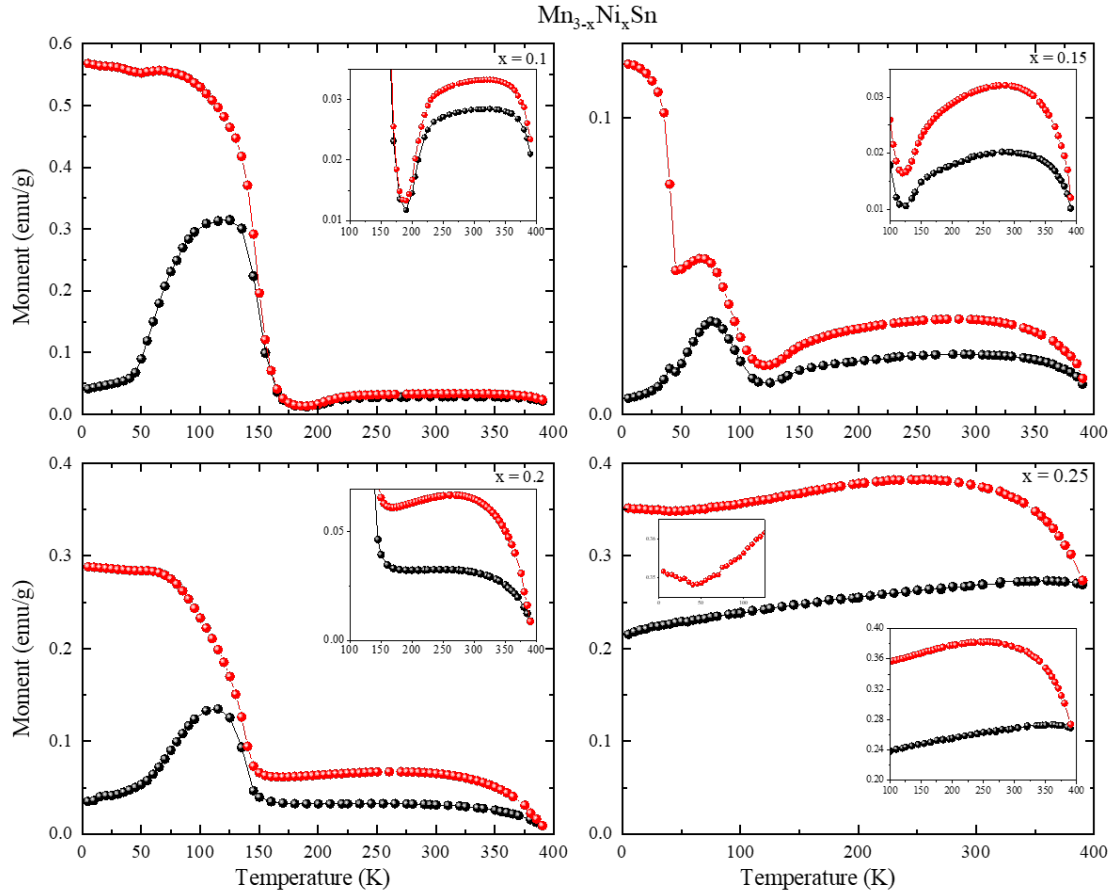


Figure 3.6: M v/s T for $\text{Mn}_{3-x}\text{Ni}_x\text{Sn}_{0.96}$, $x = 0.1, 0.15, 0.2, 0.25$

A comparison of the ZFC curves recorded for all samples in $H = 0.01\text{T}$, is presented in figure 3.7 indicated a monotonic decrease in all transition temperatures as the Ni concentration increases from $x = 0$ to $x = 0.25$. This could possibly be due to the distortion of the kagome lattice. Further analysis is in progress.

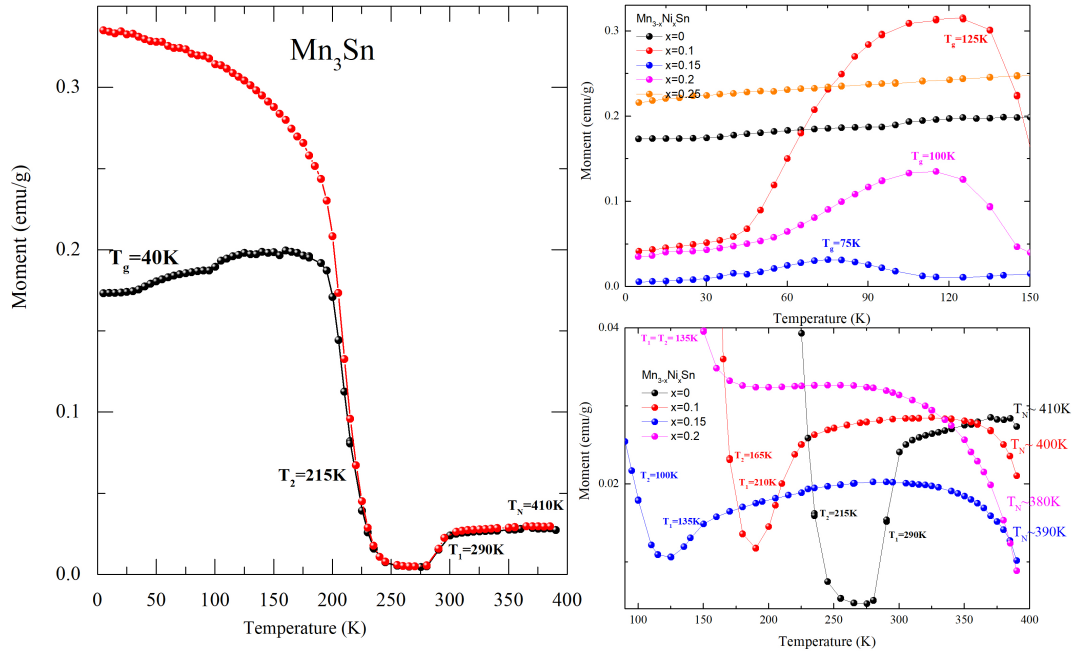


Figure 3.7: Transition Temperatures

3.3 Temperature Dependent Resistivity Measurements

Next, temperature dependent resistivity of all the samples was measured during cooling and subsequent warming cycles in the temperature range of 30K to 450K. For this, rectangular bars with dimensions in the millimetre range were cut from the sample and used. A comparison of the resistivity data with the corresponding zero field cooled magnetization curves is presented in figure 3.8.

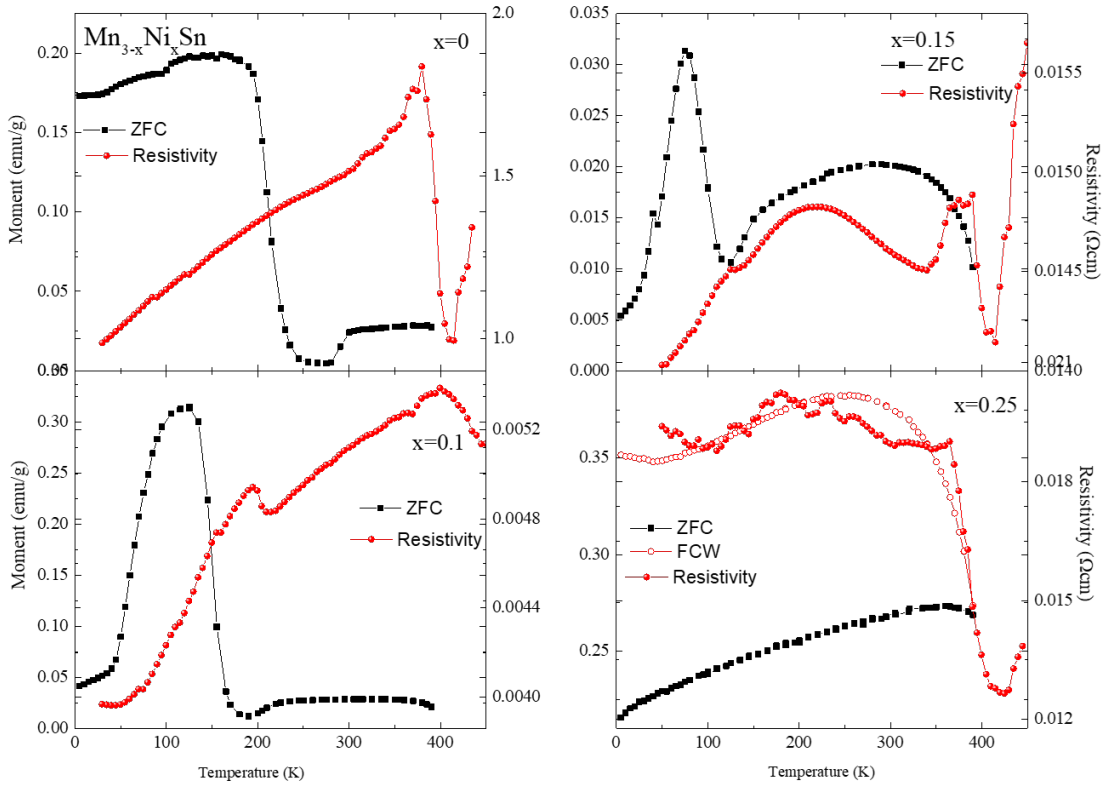


Figure 3.8: Resistivity data for $Mn_{3-x}Ni_xSn$, $x = 0.1, 0.15, 0.2, 0.25$

As seen in the figure, the Mn_3Sn alloy exhibits an overall metallic behaviour below T_N . A small kink at T_1 signals the transition from the noncollinear antiferromagnetic to a spiral magnetic state. Results from a similar study carried out on the Ni doped alloys highlight clear anomalies at temperatures corresponding to the different magnetic transitions in the ZFC magnetization curves. Therefore, in order to have a deeper understanding of the temperature dependent magnetic and transport properties exhibited in these alloys, a thorough study involving magnetization as a function of field and field dependent Hall resistivity measurements are essential.

References

- [1] Igor Žutić, Jaroslav Fabian, and S. Das Sarma. Spintronics: Fundamentals and applications. *Rev. Mod. Phys.*, 76:323–410, Apr 2004. doi: 10.1103/RevModPhys.76.323. URL <https://link.aps.org/doi/10.1103/RevModPhys.76.323>.
- [2] V. Baltz, A. Manchon, M. Tsoi, T. Moriyama, T. Ono, and Y. Tserkovnyak. Antiferromagnetic spintronics. *Rev. Mod. Phys.*, 90:015005, Feb 2018. doi: 10.1103/RevModPhys.90.015005. URL <https://link.aps.org/doi/10.1103/RevModPhys.90.015005>.
- [3] A. H. MacDonald and M. Tsoi. Antiferromagnetic metal spintronics. *Philosophical Transactions of the Royal Society A: Mathematical, Physical and Engineering Sciences*, 369(1948):3098–3114, 2011. doi: 10.1098/rsta.2011.0014. URL <https://royalsocietypublishing.org/doi/abs/10.1098/rsta.2011.0014>.
- [4] J. Železný, H. Gao, K. Výborný, J. Zemen, J. Mašek, Aurélien Manchon, J. Wunderlich, Jairo Sinova, and T. Jungwirth. Relativistic Néel-order fields induced by electrical current in antiferromagnets. *Phys. Rev. Lett.*, 113:157201, Oct 2014. doi: 10.1103/PhysRevLett.113.157201. URL <https://link.aps.org/doi/10.1103/PhysRevLett.113.157201>.
- [5] E. V. Gomonay and V. M. Loktev. Spintronics of antiferromagnetic systems (Review Article). *Low Temperature Physics*, 40(1):17–35, 01 2014. ISSN 1063-777X. doi: 10.1063/1.4862467. URL <https://doi.org/10.1063/1.4862467>.
- [6] Y. Taguchi, Y. Oohara, H. Yoshizawa, N. Nagaosa, and Y. Tokura. Spin chirality,

- Berry phase, and anomalous Hall effect in a frustrated ferromagnet. *Science*, 291(5513):2573–2576, 2001. doi: 10.1126/science.1058161. URL <https://www.science.org/doi/abs/10.1126/science.1058161>.
- [7] A. S. Núñez, R. A. Duine, Paul Haney, and A. H. MacDonald. Theory of spin torques and giant magnetoresistance in antiferromagnetic metals. *Phys. Rev. B*, 73:214426, Jun 2006. doi: 10.1103/PhysRevB.73.214426. URL <https://link.aps.org/doi/10.1103/PhysRevB.73.214426>.
- [8] Helen V. Gomonay and Vadim M. Loktev. Spin transfer and current-induced switching in antiferromagnets. *Phys. Rev. B*, 81:144427, Apr 2010. doi: 10.1103/PhysRevB.81.144427. URL <https://link.aps.org/doi/10.1103/PhysRevB.81.144427>.
- [9] A. Markou, J. M. Taylor, A. Kalache, P. Werner, S. S. P. Parkin, and C. Felser. Noncollinear antiferromagnetic Mn_3Sn films. *Phys. Rev. Mater.*, 2:051001, May 2018. doi: 10.1103/PhysRevMaterials.2.051001. URL <https://link.aps.org/doi/10.1103/PhysRevMaterials.2.051001>.
- [10] Pavel Borisov, Andreas Hochstrat, Xi Chen, Wolfgang Kleemann, and Christian Binek. Magnetoelectric switching of exchange bias. *Phys. Rev. Lett.*, 94:117203, Mar 2005. doi: 10.1103/PhysRevLett.94.117203. URL <https://link.aps.org/doi/10.1103/PhysRevLett.94.117203>.
- [11] A. B. Shick, S. Khmelevskiy, O. N. Mryasov, J. Wunderlich, and T. Jungwirth. Spin-orbit coupling induced anisotropy effects in bimetallic antiferromagnets: A route towards antiferromagnetic spintronics. *Phys. Rev. B*, 81:212409, Jun

2010. doi: 10.1103/PhysRevB.81.212409. URL <https://link.aps.org/doi/10.1103/PhysRevB.81.212409>.
- [12] S. S. P. Parkin, N. More, and K. P. Roche. Oscillations in exchange coupling and magnetoresistance in metallic superlattice structures: Co/Ru, Co/Cr, and Fe/Cr. *Phys. Rev. Lett.*, 64:2304–2307, May 1990. doi: 10.1103/PhysRevLett.64.2304. URL <https://link.aps.org/doi/10.1103/PhysRevLett.64.2304>.
- [13] P. J. H. Bloemen, H. W. van Kesteren, H. J. M. Swagten, and W. J. M. de Jonge. Oscillatory interlayer exchange coupling in Co/Ru multilayers and bilayers. *Phys. Rev. B*, 50:13505–13514, Nov 1994. doi: 10.1103/PhysRevB.50.13505. URL <https://link.aps.org/doi/10.1103/PhysRevB.50.13505>.
- [14] Robert Karplus and J. M. Luttinger. Hall effect in ferromagnetics. *Phys. Rev.*, 95:1154–1160, Sep 1954. doi: 10.1103/PhysRev.95.1154. URL <https://link.aps.org/doi/10.1103/PhysRev.95.1154>.
- [15] N A Sinitsyn. Semiclassical theories of the anomalous Hall effect. *Journal of Physics: Condensed Matter*, 20(2):023201, dec 2007. doi: 10.1088/0953-8984/20/02/023201. URL <https://dx.doi.org/10.1088/0953-8984/20/02/023201>.
- [16] A. Neubauer, C. Pfleiderer, B. Binz, A. Rosch, R. Ritz, P. G. Niklowitz, and P. Böni. Topological Hall effect in the *A* phase of MnSi. *Phys. Rev. Lett.*, 102:186602, May 2009. doi: 10.1103/PhysRevLett.102.186602. URL <https://link.aps.org/doi/10.1103/PhysRevLett.102.186602>.
- [17] N. Kanazawa, Y. Onose, T. Arima, D. Okuyama, K. Ohoyama, S. Wakimoto, K. Kakurai, S. Ishiwata, and Y. Tokura. Large topological Hall effect in a

- short-period helimagnet MnGe. *Phys. Rev. Lett.*, 106:156603, Apr 2011. doi: 10.1103/PhysRevLett.106.156603. URL <https://link.aps.org/doi/10.1103/PhysRevLett.106.156603>.
- [18] J. C. Gallagher, K. Y. Meng, J. T. Brangham, H. L. Wang, B. D. Esser, D. W. McComb, and F. Y. Yang. Robust zero-field skyrmion formation in FeGe epitaxial thin films. *Phys. Rev. Lett.*, 118:027201, Jan 2017. doi: 10.1103/PhysRevLett.118.027201. URL <https://link.aps.org/doi/10.1103/PhysRevLett.118.027201>.
- [19] F. Wolff Fabris, P. Pureur, J. Schaf, V. N. Vieira, and I. A. Campbell. Chiral anomalous Hall effect in reentrant AuFe alloys. *Phys. Rev. B*, 74:214201, Dec 2006. doi: 10.1103/PhysRevB.74.214201. URL <https://link.aps.org/doi/10.1103/PhysRevB.74.214201>.
- [20] Weifeng Zhang, Wei Han, See-Hun Yang, Yan Sun, Yang Zhang, Binghai Yan, and Stuart S. P. Parkin. Giant facet-dependent spin-orbit torque and spin Hall conductivity in the triangular antiferromagnet Mn₃Ir. *Science Advances*, 2(9): e1600759, 2016. doi: 10.1126/sciadv.1600759. URL <https://www.science.org/doi/abs/10.1126/sciadv.1600759>.
- [21] Wanxiang Feng, Guang-Yu Guo, Jian Zhou, Yugui Yao, and Qian Niu. Large magneto-optical kerr effect in noncollinear antiferromagnets Mn₃X (X = Rh, Ir, Pt). *Phys. Rev. B*, 92:144426, Oct 2015. doi: 10.1103/PhysRevB.92.144426. URL <https://link.aps.org/doi/10.1103/PhysRevB.92.144426>.
- [22] S. Mühlbauer, B. Binz, F. Jonietz, C. Pfleiderer, A. Rosch, A. Neubauer, R. Georgii, and P. Böni. Skyrmion lattice in a chiral magnet. *Science*, 323(5916):

- 915–919, 2009. doi: 10.1126/science.1166767. URL <https://www.science.org/doi/abs/10.1126/science.1166767>.
- [23] Xiaokang Li, Liangcai Xu, Linchao Ding, Jinhua Wang, Mingsong Shen, Xiufang Lu, Zengwei Zhu, and Kamran Behnia. Anomalous nernst and righi-leduc effects in Mn_3Sn : Berry curvature and entropy flow. *Phys. Rev. Lett.*, 119:056601, Aug 2017. doi: 10.1103/PhysRevLett.119.056601. URL <https://link.aps.org/doi/10.1103/PhysRevLett.119.056601>.
- [24] Hideki Narita, Muhammad Ikhlas, Motoi Kimata, Agustinus Agung Nugroho, Satoru Nakatsuji, and YoshiChika Otani. Anomalous Nernst effect in a micro-fabricated thermoelectric element made of chiral antiferromagnet Mn_3Sn . *Applied Physics Letters*, 111(20), 11 2017. ISSN 0003-6951. doi: 10.1063/1.5000815. URL <https://doi.org/10.1063/1.5000815>. 202404.
- [25] Nirmal J. Ghimire, Rebecca L. Dally, L. Poudel, D. C. Jones, D. Michel, N. Thapa Magar, M. Bleuel, Michael A. McGuire, J. S. Jiang, J. F. Mitchell, Jeffrey W. Lynn, and I. I. Mazin. Competing magnetic phases and fluctuation-driven scalar spin chirality in the kagome metal YMn_6Sn_6 . *Science Advances*, 6(51):eabe2680, 2020. doi: 10.1126/sciadv.abe2680. URL <https://www.science.org/doi/abs/10.1126/sciadv.abe2680>.
- [26] Noam Morali, Rajib Batabyal, Pranab Kumar Nag, Enke Liu, Qiunan Xu, Yan Sun, Binghai Yan, Claudia Felser, Nurit Avraham, and Haim Beidenkopf. Fermi-arc diversity on surface terminations of the magnetic Weyl semimetal $\text{Co}_3\text{Sn}_2\text{S}_2$. *Science*, 365(6459):1286–1291, 2019. doi: 10.1126/science.aav2334. URL <https://www.science.org/doi/abs/10.1126/science.aav2334>.

- [27] S. Nakatsuji, N. Kiyohara, and T. Higo. Large anomalous Hall effect in a non-collinear antiferromagnet at room temperature. *Nature*, 527:212–215, 2015. ISSN 0038-1098. doi: <https://doi.org/10.1038/nature15723>.
- [28] Ajaya K. Nayak, Julia Erika Fischer, Yan Sun, Binghai Yan, Julie Karel, Alexander C. Komarek, Chandra Shekhar, Nitesh Kumar, Walter Schnelle, Jürgen Kübler, Claudia Felser, and Stuart S. P. Parkin. Large anomalous Hall effect driven by a nonvanishing Berry curvature in the noncolinear antiferromagnet Mn_3Ge . *Science Advances*, 2(4):e1501870, 2016. doi: 10.1126/sciadv.1501870. URL <https://www.science.org/doi/abs/10.1126/sciadv.1501870>.
- [29] Zhipeng Hou, Weijun Ren, Bei Ding, Guizhou Xu, Yue Wang, Bing Yang, Qiang Zhang, Ying Zhang, Enke Liu, Feng Xu, Wenhong Wang, Guangheng Wu, Xixiang Zhang, Baogen Shen, and Zhidong Zhang. Observation of various and spontaneous magnetic skyrmionic bubbles at room temperature in a frustrated kagome magnet with uniaxial magnetic anisotropy. *Advanced Materials*, 30(7):1706306, 2018. doi: <https://doi.org/10.1002/adma.201706306>. URL <https://onlinelibrary.wiley.com/doi/abs/10.1002/adma.201706306>.
- [30] Qi Wang, Shanshan Sun, Xiao Zhang, Fei Pang, and Hechang Lei. Anomalous Hall effect in a ferromagnetic Fe_3Sn_2 single crystal with a geometrically frustrated Fe bilayer kagome lattice. *Phys. Rev. B*, 94:075135, Aug 2016. doi: 10.1103/PhysRevB.94.075135. URL <https://link.aps.org/doi/10.1103/PhysRevB.94.075135>.
- [31] M. Hirschberger, T. Nakajima, and S. Gao. Skyrmion phase and competing

- magnetic orders on a breathing kagome lattice. *Nat Commun*, 10, 2019. doi: <https://doi.org/10.1038/s41467-019-13675-4>.
- [32] Xin Chen, Hang Xie, Qi Zhang, Ziyang Luo, Lei Shen, and Yihong Wu. Giant enhancement of anomalous Hall effect in Cr modulation-doped non-collinear antiferromagnetic Mn_3Sn thin films, 2021.
- [33] Stuart S.P. Parkin. Magnetic anti-skyrmions and triangular antiferromagnetism in Mn_3X and Mn_2XY compounds. In *APS March Meeting Abstracts*, volume 2018 of *APS Meeting Abstracts*, page E05.002, January 2018.
- [34] J.M. Taylor, E. Lesne, A. Markou, F.K. Dejene, P.K. Sivakumar, S. Pöllath, K.G. Rana, N. Kumar, C. Luo, H. Ryll, F. Radu, F. Kronast, P. Werner, C.H. Back, C. Felser, and S.S.P. Parkin. Magnetic and electrical transport signatures of uncompensated moments in epitaxial thin films of the noncollinear antiferromagnet Mn_3Ir . *Applied Physics Letters*, 115(6), 08 2019. ISSN 0003-6951. doi: 10.1063/1.5099428. URL <https://doi.org/10.1063/1.5099428>. 062403.
- [35] J.M. Taylor, E. Lesne, A. Markou, F.K. Dejene, B. Ernst, A. Kalache, K.G. Rana, N. Kumar, P. Werner, C. Felser, and S.S.P. Parkin. Epitaxial growth, structural characterization, and exchange bias of noncollinear antiferromagnetic Mn_3Ir thin films. *Phys. Rev. Mater.*, 3:074409, Jul 2019. doi: 10.1103/PhysRevMaterials.3.074409. URL <https://link.aps.org/doi/10.1103/PhysRevMaterials.3.074409>.
- [36] F. Theuss, S. Ghosh, T. Chen, O. Tchernyshyov, S. Nakatsuji, and B.J. Ramshaw. Strong magnetoelastic coupling in Mn_3X ($\text{X} = \text{Ge}, \text{Sn}$). *Phys. Rev. B*, 105:174430,

- May 2022. doi: 10.1103/PhysRevB.105.174430. URL <https://link.aps.org/doi/10.1103/PhysRevB.105.174430>.
- [37] F. Hu, G. Xu, Y. You, Z. Zhang, Z. Xu, Y. Gong, E. Liu, H. Zhang, E. Liu, W. Wang, and F. Xu. Tunable magnetic and transport properties of Mn_3Ga thin films on Ta/Ru seed layer. *Journal of Applied Physics*, 123(10), 03 2018. ISSN 0021-8979. doi: 10.1063/1.5005895. URL <https://doi.org/10.1063/1.5005895>. 103902.
- [38] Helena Reichlova, Tomas Janda, Joao Godinho, Anastasios Markou, Dominik Kriegner, Richard Schlitz, Jakub Zelezny, Zbynek Soban, Mauricio Bejarano, Helmut Schultheiss, Petr Nemeč, Tomas Jungwirth, Claudia Felser, Joerg Wunderlich, and Sebastian T. B. Goennenwein. Imaging and writing magnetic domains in the non-collinear antiferromagnet Mn_3Sn . *Nature Communications*, 10(1):5459, Nov 2019. ISSN 2041-1723. doi: 10.1038/s41467-019-13391-z. URL <https://doi.org/10.1038/s41467-019-13391-z>.
- [39] Muhammad Ikhlas, Takahiro Tomita, Takashi Koretsune, Michi-To Suzuki, Daisuke Nishio-Hamane, Ryotaro Arita, Yoshichika Otani, and Satoru Nakatsuji. Large anomalous nernst effect at room temperature in a chiral antiferromagnet. *Nature Physics*, 13(11):1085–1090, Nov 2017. ISSN 1745-2481. doi: 10.1038/nphys4181. URL <https://doi.org/10.1038/nphys4181>.
- [40] K. Kuroda, T. Tomita, M.-T. Suzuki, C. Bareille, A. A. Nugroho, P. Goswami, M. Ochi, M. Ikhlas, M. Nakayama, S. Akebi, R. Noguchi, R. Ishii, N. Inami, K. Ono, H. Kumigashira, A. Varykhalov, T. Muro, T. Koretsune, R. Arita, S. Shin, Takeshi Kondo, and S. Nakatsuji. Evidence for magnetic Weyl fermions

- in a correlated metal. *Nature Materials*, 16(11):1090–1095, Nov 2017. ISSN 1476-4660. doi: 10.1038/nmat4987. URL <https://doi.org/10.1038/nmat4987>.
- [41] J. Kübler and C. Felser. Non-collinear antiferromagnets and the anomalous Hall effect. *Europhysics Letters*, 108(6):67001, dec 2014. doi: 10.1209/0295-5075/108/67001. URL <https://dx.doi.org/10.1209/0295-5075/108/67001>.
- [42] Jianpeng Liu and Leon Balents. Anomalous Hall effect and topological defects in antiferromagnetic Weyl semimetals: $\text{Mn}_3\text{Sn}/\text{Ge}$. *Phys. Rev. Lett.*, 119:087202, Aug 2017. doi: 10.1103/PhysRevLett.119.087202. URL <https://link.aps.org/doi/10.1103/PhysRevLett.119.087202>.
- [43] Hao Yang, Yan Sun, Yang Zhang, Wu-Jun Shi, Stuart S P Parkin, and Binghai Yan. Topological Weyl semimetals in the chiral antiferromagnetic materials Mn_3Ge and Mn_3Sn . *New Journal of Physics*, 19(1):015008, jan 2017. doi: 10.1088/1367-2630/aa5487. URL <https://dx.doi.org/10.1088/1367-2630/aa5487>.
- [44] Tomoya Higo, Huiyuan Man, Daniel B. Gopman, Liang Wu, Takashi Koretsune, Olaf M. J. van 't Erve, Yury P. Kabanov, Dylan Rees, Yufan Li, Michito Suzuki, Shreyas Patankar, Muhammad Ikhlas, C. L. Chien, Ryotaro Arita, Robert D. Shull, Joseph Orenstein, and Satoru Nakatsuji. Large magneto-optical kerr effect and imaging of magnetic octupole domains in an antiferromagnetic metal. *Nature Photonics*, 12(2):73–78, Feb 2018. ISSN 1749-4893. doi: 10.1038/s41566-017-0086-z. URL <https://doi.org/10.1038/s41566-017-0086-z>.
- [45] Motoi Kimata, Hua Chen, Kouta Kondou, Satoshi Sugimoto, Prasanta K. Muduli, Muhammad Ikhlas, Yasutomo Omori, Takahiro Tomita, Allan. H. Mac-

- Donald, Satoru Nakatsuji, and Yoshichika Otani. Magnetic and magnetic inverse spin Hall effects in a non-collinear antiferromagnet. *Nature*, 565(7741): 627–630, Jan 2019. ISSN 1476-4687. doi: 10.1038/s41586-018-0853-0. URL <https://doi.org/10.1038/s41586-018-0853-0>.
- [46] J. Yan, X. Luo, H. Y. Lv, Y. Sun, P. Tong, W. J. Lu, X. B. Zhu, W. H. Song, and Y. P. Sun. Room-temperature angular-dependent topological Hall effect in chiral antiferromagnetic Weyl semimetal Mn_3Sn . *Applied Physics Letters*, 115(10):102404, 2019. doi: 10.1063/1.5119838. URL <https://doi.org/10.1063/1.5119838>.
- [47] Y. Song, Y. Hao, S. Wang, J. Zhang, Q. Huang, X. Xing, and J. Chen. Complicated magnetic structure and its strong correlation with the anomalous Hall effect in Mn_3Sn . *Phys. Rev. B*, 101:144422, Apr 2020. doi: 10.1103/PhysRevB.101.144422. URL <https://link.aps.org/doi/10.1103/PhysRevB.101.144422>.
- [48] T.F. Duan, W.J. Ren, and et al. Magnetic anisotropy of single-crystalline Mn_3Sn in triangular and helix-phase states. *Applied Physics Letters*, 107(8):082403, 2015. doi: 10.1063/1.4929447. URL <https://doi.org/10.1063/1.4929447>.
- [49] A. Zelenskiy, T.L. Monchesky, M.L. Plumer, and B.W. Southern. Anisotropic magnetic interactions in hexagonal *ab*-stacked kagome lattice structures: Application to Mn_3X ($X = Ge, Sn, Ga$) compounds. *Phys. Rev. B*, 103:144401, Apr 2021. doi: 10.1103/PhysRevB.103.144401. URL <https://link.aps.org/doi/10.1103/PhysRevB.103.144401>.
- [50] James Mark Taylor. *Epitaxial thin films of the noncollinear antiferromagnets Mn_3Ir and Mn_3Sn for topological spintronic applications*. PhD thesis,

- Martin-Luther-University Halle-Wittenberg, 2020. URL <http://dx.doi.org/10.25673/34685>.
- [51] S. Tomiyoshi and Y. Yamaguchi. Magnetic structure and weak ferromagnetism of Mn_3Sn studied by polarized neutron diffraction. *Journal of the Physical Society of Japan*, 51(8):2478–2486, 1982. doi: 10.1143/JPSJ.51.2478. URL <https://doi.org/10.1143/JPSJ.51.2478>.
- [52] J. Liu and L. Balents. Anomalous Hall effect and topological defects in antiferromagnetic Weyl semimetals: $\text{Mn}_3\text{Sn}/\text{Ge}$. *Phys. Rev. Lett.*, 119:087202, Aug 2017. doi: 10.1103/PhysRevLett.119.087202. URL <https://link.aps.org/doi/10.1103/PhysRevLett.119.087202>.
- [53] T. Nagamiya, S. Tomiyoshi, and Y. Yamaguchi. Triangular spin configuration and weak ferromagnetism of Mn_3Sn and Mn_3Ge . *Solid State Communications*, 42(5):385–388, 1982. ISSN 0038-1098. doi: [https://doi.org/10.1016/0038-1098\(82\)90159-4](https://doi.org/10.1016/0038-1098(82)90159-4). URL <https://www.sciencedirect.com/science/article/pii/0038109882901594>.
- [54] P. Park, J. Oh, K. Uhlířová, and et al. Magnetic excitations in non-collinear antiferromagnetic Weyl semimetal Mn_3Sn . *npj Quantum Materials*, 3(63), 2018. doi: <https://doi.org/10.1038/s41535-018-0137-9>.
- [55] J.W. Cable, N. Wakabayashi, and RadhakrishnaP. A neutron study of the magnetic structure of Mn_3Sn . *Solid State Communications*, 88(2):161–166, 1993. ISSN 0038-1098. doi: [https://doi.org/10.1016/0038-1098\(93\)90400-H](https://doi.org/10.1016/0038-1098(93)90400-H). URL <https://www.sciencedirect.com/science/article/pii/003810989390400H>.

- [56] H. Ohmori, S. Tomiyoshi, H. Yamauchi, and H. Yamamoto. Spin structure and weak ferromagnetism of Mn_3Sn . *Journal of Magnetism and Magnetic Materials*, 70(1):249–251, 1987. ISSN 0304-8853. doi: [https://doi.org/10.1016/0304-8853\(87\)90427-6](https://doi.org/10.1016/0304-8853(87)90427-6). URL <https://www.sciencedirect.com/science/article/pii/0304885387904276>.
- [57] W.J. Feng, D. Li, W.J. Ren, Y.B. Li, W.F. Li, J. Li, Y.Q. Zhang, and Z.D. Zhang. Glassy ferromagnetism in Ni_3Sn -type $\text{Mn}_{3.1}\text{Sn}_{0.9}$. *Phys. Rev. B*, 73:205105, May 2006. doi: 10.1103/PhysRevB.73.205105. URL <https://link.aps.org/doi/10.1103/PhysRevB.73.205105>.
- [58] N. H. Sung, F. Ronning, J. D. Thompson, and E. D. Bauer. Magnetic phase dependence of the anomalous Hall effect in Mn_3Sn single crystals. *Applied Physics Letters*, 112(13):132406, 2018. doi: 10.1063/1.5021133. URL <https://doi.org/10.1063/1.5021133>.
- [59] S. Tomiyoshi, H. Yoshida, H. Ohmori, T. Kaneko, and H. Yamamoto. Electrical properties of the intermetallic compound Mn_3Sn . *Journal of Magnetism and Magnetic Materials*, 70(1):247–248, 1987. ISSN 0304-8853. doi: [https://doi.org/10.1016/0304-8853\(87\)90426-4](https://doi.org/10.1016/0304-8853(87)90426-4). URL <https://www.sciencedirect.com/science/article/pii/0304885387904264>.
- [60] Xiao Wang. *Single crystal growth and neutron scattering studies of novel quantum materials*. PhD thesis, RWTH Aachen, Feb 2021. URL http://inis.iaea.org/search/search.aspx?orig_q=RN:53047079. Available from INIS: http://inis.iaea.org/search/search.aspx?orig_q=RN:53047079; Available from

- INIS in electronic form. Also available from: <http://dx.doi.org/10.18154/RWTH-2021-04916>.
- [61] A. Low, S. Ghosh, S. Changdar, S. Routh, S. Purwar, and S. Thirupathaiah. Tuning of topological properties in the strongly correlated antiferromagnet Mn_3Sn via Fe doping. *Phys. Rev. B*, 106:144429, Oct 2022. doi: 10.1103/PhysRevB.106.144429. URL <https://link.aps.org/doi/10.1103/PhysRevB.106.144429>.
- [62] Xiaoyan Yang, Yi Qiu, Jie Su, Yalei Huang, Jincang Zhang, Xiao Liang, and Guixin Cao. Coexistence of in-plane and out-of-plane exchange bias in correlated kagome antiferromagnet $\text{Mn}_{3-x}\text{Cr}_x\text{Sn}$, 2022.
- [63] C. Kittel. *Introduction to Solid State Physics*. John-Wiley and Sons, Inc, 2005. ISBN 0-471-41526-X.
- [64] N.W. Ashcroft and N.D. Mermin. *Solid State Physics*. Saunders College Publishing, 1976. ISBN 0-03-083993-9.
- [65] H.M. Rietveld. A profile refinement method for nuclear and magnetic structures. *Journal of Applied Crystallography*, 2(2):65–71, Jun 1969. doi: 10.1107/S0021889869006558. URL <https://doi.org/10.1107/S0021889869006558>.
- [66] R. Srinivasan, K.R. Priolkar, and T.G. Ramesh. *A Manual on Experiments in Physics*. Indian Academy of Sciences, 2018.